Geoscientific
Model Development

Open Access

The Yale Interactive terrestrial Biosphere model version 1.0: description, evaluation and implementation into NASA GISS ModelE2

X. Yue and N. Unger

School of Forestry and Environment Studies, Yale University, New Haven, Connecticut 06511, USA

Correspondence to: X. Yue (xuyueseas@gmail.com)

Abstract. The land biosphere, atmospheric chemistry and climate are intricately interconnected, yet the modeling of carbon–climate and chemistry–climate interactions have evolved as entirely separate research communities. We describe the Yale Interactive terrestrial Biosphere (YIBs) model version 1.0, a land carbon cycle model that has been developed for coupling to the NASA Goddard Institute for Space Studies (GISS) ModelE2 global chemistry–climate model. The YIBs model adapts routines from the mature TRIFFID (Top-down Representation of Interactive Foliage and Flora Including Dynamics) and CASA (Carnegie–Ames–Stanford Approach) models to simulate interactive carbon assimilation, allocation, and autotrophic and heterotrophic respiration. Dynamic daily leaf area index is simulated based on carbon allocation and temperature- and drought-dependent prognostic phenology. YIBs incorporates a semi-mechanistic ozone vegetation damage scheme. Here, we validate the present-day YIBs land carbon fluxes for three increasingly complex configurations: (i) offline local site level, (ii) offline global forced with WFDEI (WATCH Forcing Data methodology applied to ERA-Interim data) meteorology, and (iii) online coupled to the NASA ModelE2 (NASA ModelE2-YIBs). Offline YIBs has hourly and online YIBs has half-hourly temporal resolution. The large observational database used for validation includes carbon fluxes from 145 flux tower sites and multiple satellite products. At the site level, YIBs simulates reasonable seasonality (correlation coefficient $R > 0.8$) of gross primary productivity (GPP) at 121 out of 145 sites with biases in magnitude ranging from -19 to 7% depending on plant functional type. On the global scale, the offline model simulates an annual GPP of 125 ± 3 Pg C and net ecosystem exchange (NEE) of -2.5 ± 0.7 Pg C for 1982–2011, with seasonality and spatial distribution consistent with the satellite observations. We assess present-day global ozone vegetation damage using the offline YIBs configuration. Ozone damage reduces global GPP by 2–5 % annually with regional extremes of 4–10 % in east Asia. The online model simulates annual GPP of 123 ± 1 Pg C and NEE of -2.7 ± 0.7 Pg C. NASA ModelE2-YIBs is a useful new tool to investigate coupled interactions between the land carbon cycle, atmospheric chemistry, and climate change.

1 Introduction

The terrestrial biosphere interacts with the atmosphere through the exchanges of energy, carbon, reactive gases, water, and momentum fluxes. Forest ecosystems absorb an estimated 120 Pg C year^{-1} from the atmosphere (Beer et al., 2010) and mitigate about one-quarter of the anthropogenic carbon dioxide (CO_2) emissions (Friedlingstein et al., 2014). This carbon assimilation is sensitive to human-caused perturbations including climate change and land use change (Zhao and Running, 2010; Houghton et al., 2012) and is affected by atmospheric pollutants such as ozone and aerosols (Sitch et al., 2007; Mercado et al., 2009). Over the past 2–3 decades, a number of terrestrial biosphere models have been developed as tools to quantify the present-day global carbon budget in conjunction with available but sparse observations (e.g., Jung et al., 2009), to understand the relationships between terrestrial biospheric fluxes and environmental conditions (e.g., Zeng et al., 2005), to attribute drivers of trends in the carbon cycle during the anthropogenic era (e.g., Sitch et al., 2015),

and to project future changes in the land biosphere and the consequences for regional and global climate change (e.g., Friedlingstein et al., 2006).

Emerging research identifies climatically relevant interactions between the land biosphere and atmospheric chemistry (e.g, Huntingford et al., 2011). For instance, stomatal uptake is an important sink of tropospheric ozone (Val Martin et al., 2014) but damages photosynthesis, reduces plant growth and biomass accumulation, limits crop yields, and affects stomatal control over plant transpiration of water vapor between the leaf surface and atmosphere (Ainsworth et al., 2012; Hollaway et al., 2012). The indirect CO_2 radiative forcing due to the vegetation damage effects of anthropogenic ozone increases since the industrial revolution may be as large as $+0.4\,W\,m^{-2}$ (Sitch et al., 2007), which is 25 % of the magnitude of the direct CO_2 radiative forcing over the same period, and of similar magnitude to the direct ozone radiative forcing. Atmospheric oxidation of biogenic volatile organic compound (BVOC) emissions affects surface air quality and exerts additional regional and global chemical climate forcings (Scott et al., 2014; Unger, 2014a, b). Fine-mode atmospheric pollution particles affect the land biosphere by changing the physical climate state and through diffuse radiation fertilization (Mercado et al., 2009; Mahowald, 2011). Land plant phenology has experienced substantial changes in the last few decades (Keenan et al., 2014), possibly influencing both ozone deposition and BVOC emissions through the extension of growing seasons. These coupled interactions are often not adequately represented in current generation land biosphere models or global chemistry–climate models. Global land carbon cycle models often prescribe offline ozone and aerosol fields (e.g., Sitch et al., 2007; Mercado et al., 2009), and global chemistry–climate models often prescribe fixed offline vegetation fields (e.g., Lamarque et al., 2013; Shindell et al., 2013a). However, multiple mutual feedbacks occur between vegetation physiology and reactive atmospheric chemical composition that are completely neglected using these previous offline approaches. Model frameworks are needed that fully two-way couple the land carbon cycle and atmospheric chemistry and simulate the consequences for climate change.

Our objective is to present the description and present-day evaluation of the Yale Interactive terrestrial Biosphere (YIBs) model version 1.0 that has been developed for the investigation of carbon–chemistry–climate interactions. The YIBs model can be used in three configurations: (i) offline local site level, (ii) offline global forced with WFDEI (WATCH Forcing Data methodology applied to ERA-Interim data) meteorology, and (iii) online coupled to the latest frozen version of the NASA GISS (Goddard Institute for Space Studies) ModelE2 (Schmidt et al., 2014). The global climate model represents atmospheric gas-phase and aerosol chemistry, cloud, radiation, and land surface processes, and has been widely used for studies of atmospheric components, climate change, and their interactions (Schmidt et al., 2006;

Koch et al., 2011; Unger, 2011; Shindell et al., 2013b; Miller et al., 2014). To our knowledge, this study represents the first description and validation of an interactive climate-sensitive closed land carbon cycle in NASA ModelE2. The impacts of the updated vegetation scheme on the chemistry and climate simulations in NASA ModelE2 will be addressed in other ongoing research. Section 2 describes the observational data sets used to evaluate YIBs land carbon cycle performance. Section 3 describes physical parameterizations of the vegetation model. Section 4 explains the model setup and simulations in three configurations. Section 5 presents the results of the model evaluation and Sect. 6 summarizes the model performance.

YIBs design strategy

Many land carbon cycle models already exist (e.g., Sitch et al., 2015, and references therein; Schaefer et al., 2012, and references therein). We elected to build YIBs in a step-by-step process such that our research group has intimate familiarity with the underlying scientific processes, rather than adopting an existing model as a "black box". This unconventional interdisciplinary approach is important for discerning the complex mutual feedbacks between atmospheric chemistry and the land carbon sink under global change. The development of the YIBs land carbon cycle model has proceeded in three main steps. The first step was the implementation of vegetation biophysics, photosynthesis-dependent BVOC emissions and ozone vegetation damage that have been extensively documented, validated and applied in seven previous publications (Unger, 2013, 2014a, b; Unger et al., 2013; Unger and Yue, 2014; Yue and Unger, 2014; Zheng et al., 2015). The second step was the selection of the YIBs default phenology scheme based on rigorous intercomparison of 13 published phenological models (Yue et al., 2015a). This study represents the third step to simulate the closed climate-sensitive land carbon cycle: implementation of interactive carbon assimilation, allocation, autotrophic and heterotrophic respiration, and dynamic tree growth (changes in both height and LAI). For this third step, we purposefully select the mature, well-supported, well-established, readily available and accessible community algorithms: TRIFFID (Top-down Representation of Interactive Foliage and Flora Including Dynamics; Cox, 2001; Clark et al., 2011) and the Carnegie–Ames–Stanford Approach (CASA) (Potter et al., 1993; Schaefer et al., 2008). TRIFFID has demonstrated previous usability in carbon–chemistry–climate interactions research.
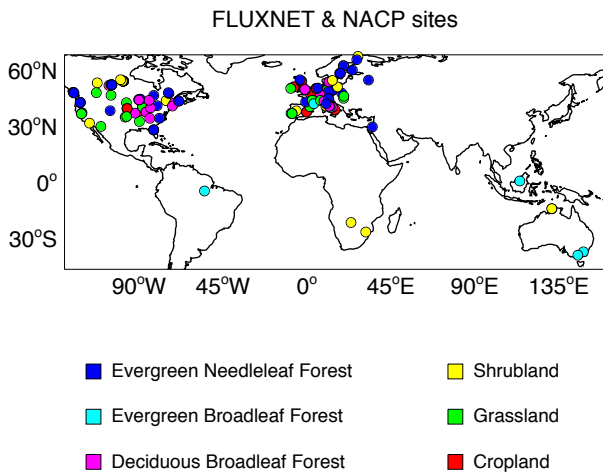
FLUXNET & NACP sites

Figure 1. Distribution of 145 sites from the FLUXNET and the North American Carbon Program (NACP) network. The duplicated sites have been removed. The color indicates different plant functional types (PFTs) as evergreen needleleaf forest (ENF, blue), evergreen broadleaf forest (EBF, cyan), deciduous broadleaf forest (DBF, magenta), shrubland (SHR, yellow) grassland (GRA, green), and cropland (CRO, red). "mixed forests" are classified as ENF, "permanent wetlands", "savannas", and "woody savannas" as SHR. The PFT of each site is described in Table S1 in the Supplement.

2 Observational data sets for validation

2.1 Site-level measurements

To validate the YIBs model, we use eddy covariance measurements from 145 flux tower sites (Fig. 1), which are collected by the North American Carbon Program (Schaefer et al., 2012) (K. Schaefer, personal communication, 2013) and downloaded from the FLUXNET (http://fluxnet.ornl.gov) network. Among these sites, 138 are located in the Northern Hemisphere, with 74 in Europe, 38 in the USA, and 24 in Canada (Table S1 in the Supplement). Sites on other continents are limited. Most of the sites have one dominant plant functional type (PFT), including 54 sites of evergreen needleleaf forests (ENF), 20 deciduous broadleaf forests (DBF), 9 evergreen broadleaf forests (EBF), 28 grasslands, 18 shrublands, and 16 croplands. We attribute sites with mixed forest to the ENF as these sites are usually at high latitudes. Each site's data set provides hourly or half-hourly measurements of carbon fluxes, including gross primary productivity (GPP) and net ecosystem exchange (NEE), and CO_2 concentrations and meteorological variables, such as surface air temperature, relative humidity, wind speed, and shortwave radiation.

2.2 Global measurements

We use global tree height, leaf area index (LAI), GPP, net primary productivity (NPP), and phenology data sets to validate the vegetation model. Canopy height is retrieved using

2005 remote sensing data from the Geoscience Laser Altimeter System (GLAS) aboard the ICESat satellite (Simard et al., 2011). LAI measurements for 1982–2011 are derived using the normalized difference vegetation index (NDVI) from Global Inventory Modeling and Mapping Studies (GIMMS; Zhu et al., 2013). Global GPP observations of 1982–2011 are estimated based on the upscaling of FLUXNET eddy covariance data with a biosphere model (Jung et al., 2009). This product was made to reproduce a model (LPJmL, Lund–Potsdam–Jena managed Land) using the fraction of absorbed PAR simulated in LPJmL. As a comparison, we also use GPP observations of 1982–2008 derived based on FLUXNET, satellite, and meteorological observations (Jung et al., 2011), which are about 10 % lower than those of Jung et al. (2009). The NPP for 2000–2011 is derived using remote sensing data from Moderate Resolution Imaging Spectroradiometer (MODIS) (Zhao et al., 2005). We use the global retrieval of greenness onset derived from the Advanced Very High Resolution Radiometer (AVHRR) and the MODIS data from 1982 to 2011 (Zhang et al., 2014). All data sets are interpolated to the $1° \times 1°$ offline model resolution for comparisons.

3 YIBs model description

3.1 Vegetation biophysics

YIBs calculates carbon uptake for 9 PFTs: tundra, C3/C4 grass, shrubland, DBF, ENF, EBF, and C3/C4 cropland (Table 1). In the gridded large-scale model applications, each model PFT fraction in the vegetated part of each grid cell represents a single canopy. The vegetation biophysics simulates C3 and C4 photosynthesis with the well-established Michaelis–Menten enzyme-kinetics scheme (Farquhar et al., 1980; von Caemmerer and Farquhar, 1981) and the stomatal conductance model of Ball and Berry (Ball et al., 1987). The total leaf photosynthesis (A_{tot}, µmol m^{-2} [leaf] s^{-1}) is limited by one of three processes: (i) the capacity of the ribulose 1,5-bisphosphate (RuBP) carboxylase/oxygenase enzyme (rubisco) to catalyze carbon fixation (J_c), (ii) the capacity of the Calvin cycle and the thylakoid reactions to regenerate RuBP supported by electron transport (J_e), and (iii) the capacity of starch and sucrose synthesis to regenerate inorganic phosphate for photo-phosphorylation in C3 plants and phosphoenolpyruvate (PEP) in C4 plants (J_s).

$$A_{tot} = \min(J_c, J_e, J_s) \tag{1}$$

The J_c, J_e, and J_s are parameterized as functions of environmental variables (e.g., temperature, radiation, and CO_2 concentrations) and the maximum carboxylation capacity (V_{cmax}, µmol m^{-2} s^{-1}) (Collatz et al., 1991, 1992):

$$J_c = \begin{cases} V_{cmax}\left(\dfrac{c_i - \Gamma_*}{c_i + K_c(1 + O_i/K_o)}\right) & \text{for C3 plant} \\ V_{cmax} & \text{for C4 plant} \end{cases} \tag{2}$$

Table 1. Photosynthetic and allometric parameters for the vegetation model.

PFT [*]	TDA	GRAC3	GRAC4	SHR	DBF	ENF	EBF	CROC3	CROC4
Carboxylation	C3	C3	C4	C3	C3	C3	C3	C3	C4
V_{cmax25} (μmol m^{-2} s^{-1})	33	43	24	38	45	43	40	40	40
m	9	9	5	9	9	9	9	11	5
b (mmol m^{-2} s^{-1})	2	2	2	2	2	2	2	8	2
a_{wl} (kg C m^{-2})	0.1	0.005	0.005	0.1	0.95	0.85	0.95	0.005	0.005
b_{wl}	1.667	1.667	1.667	1.667	1.667	1.667	1.667	1.667	1.667
σ_l (kg C m^{-2} LAI^{-1})	0.05	0.025	0.05	0.05	0.0375	0.1	0.0375	0.025	0.05
η (kg C m^{-1} LAI^{-1})	0.01	0.01	0.01	0.01	0.01	0.01	0.01	0.01	0.01
n_0 (kg N [kg C]$^{-1}$)	0.06	0.073	0.06	0.06	0.046	0.033	0.046	0.073	0.06
n_{rl}	0.5	1	1	0.5	0.5	0.75	0.5	1	1
n_{wl}	0.1	1	1	0.1	0.1	0.1	0.1	1	1
r_g	0.2	0.2	0.2	0.2	0.2	0.2	0.2	0.2	0.2
LAI$_{min}$	1	1	1	1	1	1	1	1	1
LAI$_{max}$	3	3	3	3	9	5	9	3	3
γ_r (360 days)$^{-1}$	0.5	0.75	0.75	0.5	0.75	0.25	0.75	0.75	0.75
γ_w (360 days)$^{-1}$	0.1	0.2	0.2	0.1	0.015	0.01	0.015	0.2	0.2
H_0 (m)	1	0.8	1.3	1	19	16.5	19	0.8	1.3

[*] Plant functional types (PFTs) are tundra (TDA), C3 grassland (GRAC3), C4 savanna/grassland (GRAC4), shrubland (SHR), deciduous broadleaf forest (DBF), evergreen needleleaf forest (ENF), evergreen broadleaf forest (EBF), and C3/C4 cropland (CROC3/CROC4).

$$J_e = \begin{cases} a_{leaf} \times PAR \times \alpha \times \left(\dfrac{c_i - \Gamma_*}{c_i + 2\Gamma_*} \right) & \text{for C3 plant}, \\ a_{leaf} \times PAR \times \alpha & \text{for C4 plant} \end{cases} \quad (3)$$

$$J_s = \begin{cases} 0.5 V_{cmax} & \text{for C3 plant} \\ K_s \times V_{cmax} \times \dfrac{c_i}{P_s} & \text{for C4 plant'} \end{cases} \quad (4)$$

where c_i and O_i are the leaf internal partial pressure (Pa) of CO_2 and oxygen, Γ_* (Pa) is the CO_2 compensation point, and K_c and K_o (Pa) are Michaelis–Menten parameters for the carboxylation and oxygenation of rubisco. The parameters K_c, K_o, and Γ_* vary with temperature according to a Q_{10} function. PAR (μmol m^{-2} s^{-1}) is the incident photosynthetically active radiation, a_{leaf} is leaf-specific light absorbance, and α is intrinsic quantum efficiency. P_s is the ambient pressure and K_s is a constant set to 4000 following Oleson et al. (2010). V_{cmax} is a function of the optimal V_{cmax} at 25 °C (V_{cmax25}) based on a Q_{10} function.

Net carbon assimilation (A_{net}) of leaf is given by

$$A_{net} = A_{tot} - R_d, \quad (5)$$

where R_d is the rate of dark respiration set to 0.011 V_{cmax} for C3 plants (Farquhar et al., 1980) and 0.025 V_{cmax} for C4 plants (Clark et al., 2011). The stomatal conductance of water vapor (g_s in mol [H_2O] m^{-2} s^{-1}) is dependent on net photosynthesis:

$$g_s = m \frac{A_{net} \times RH}{c_s} + b, \quad (6)$$

where m and b are the slope and intercept derived from empirical fitting to the Ball and Berry stomatal conductance equations, RH is relative humidity, and c_s is the CO_2 concentration at the leaf surface. In the model, the slope m is influenced by water stress, so that drought decreases photosynthesis by affecting stomatal conductance. Appropriate photosynthesis parameters for different PFTs are taken from Friend and Kiang (2005) and the Community Land Model (Oleson et al., 2010) with updates from Bonan et al. (2011) (Table 1). In future work, we will investigate the carbon–chemistry–climate impacts of updated stomatal conductance models in YIBs (Berry et al., 2010; Pieruschka et al., 2010; Medlyn et al., 2011).

The coupled equation system of photosynthesis, stomatal conductance and CO_2 diffusive flux transport equations form a cube in A_{net} that is solved analytically (Baldocchi, 1994). A simplified but realistic representation of soil water stress β is included in the vegetation biophysics following the approach of Porporato et al. (2001). The algorithm reflects the relationship between soil water amount and the extent of stomatal closure ranging from no water stress to the soil moisture stress onset point (s^*) through to the wilting point (s_{wilt}). Stomatal conductance is reduced linearly between the PFT-specific values of s^* and s_{wilt} based on the climate model's soil water volumetric saturation in six soil layers (Unger et al., 2013).

The canopy radiative transfer scheme divides the canopy into an adaptive number of layers (typically 2–16) for light stratification. Each canopy layer distinguishes sunlit and shaded portions of leaves, so that the direct and diffuse photosynthetically active radiation (PAR) is used for carbon as-

simlation respectively (Spitters et al., 1986). The leaf photosynthesis is then integrated over all canopy layers to generate the GPP:

$$\text{GPP} = \int_0^{\text{LAI}} A_{\text{tot}} dL. \tag{7}$$

3.2 Leaf phenology

Phenology determines the annual cycle of LAI. Plant phenology is generally controlled by temperature, water availability, and photoperiod (Richardson et al., 2013). For deciduous trees, the timing of budburst is sensitive to temperature (Vitasse et al., 2009) and the autumn senescence is related to both temperature and photoperiod (Delpierre et al., 2009). For small trees and grasses, such as tundra, savanna, and shrubland, phenology is controlled by temperature and/or soil moisture, depending on the species type and locations of the vegetation (Delbart and Picard, 2007; Liu et al., 2013). In the YIBs model, leaf phenology is updated on a daily basis. For the YIBs model, we build on the phenology scheme of Kim et al. (2015) and extend it based on long-term measurements of leaf phenology at five US sites (Yue et al., 2015a, hereinafter Y2015) and GPP at the 145 flux tower sties. A summary of the phenological parameters adopted is listed in Table 2.

3.2.1 Deciduous broadleaf forest (DBF)

We predict spring phenology of DBF using the cumulative thermal summation (White et al., 1997). The accumulative growing degree day (GDD) is calculated for the nth day from winter solstice if the 10-day average air temperature T_{10} is higher than a base temperature T_b:

$$\text{GDD} = \sum_{i=1}^{n} \max(T_{10} - T_b, 0). \tag{8}$$

Here T_b is set to 5 °C as in Murray et al. (1989). Similar to the approach outlined in Kim et al. (2015), the onset of greenness is triggered if the GDD exceeds a threshold value G_b and a temperature-dependent phenological factor f_T is calculated as follows:

$$f_T = \begin{cases} \min\left(1, \dfrac{\text{GDD} - G_b}{L_g}\right), & \text{if GDD} \geq G_b \\ 0, & \text{otherwise} \end{cases} \tag{9}$$

Following Murray et al. (1989), the threshold $G_b = a + b\exp(r \times \text{NCD})$ is dependent on the number of chill days (NCD), which is calculated as the total days with < 5 °C from winter solstice.

The autumn phenology is more uncertain than budburst because it is affected by both temperature and photoperiod (White et al., 1997; Delpierre et al., 2009). For the
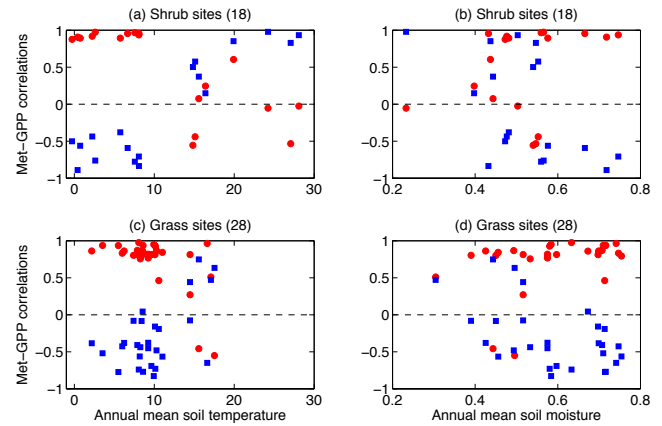

Figure 2. Correlations between monthly GPP and soil variables at **(a, b)** shrub and **(c, d)** grass sites. For each site, we calculate correlation coefficients of GPP–soil temperature (red points) and GPP–soil moisture (blue squares). These correlation coefficients are then plotted against the annual mean **(a, c)** soil temperature (°C) or **(b, d)** soil moisture (fraction) at each site.

temperature-dependent phenology, we adopted the cumulative cold summation method (Dufrene et al., 2005; Richardson et al., 2006), which calculates the accumulative falling degree day (FDD) for the mth day from summer solstice as follows:

$$\text{FDD} = \sum_{i=1}^{m} \min(T_{10} - T_s, 0), \tag{10}$$

where T_s is 20 °C as in Dufrene et al. (2005). Similar to the budburst process, we determine the autumn phenological factor based on a fixed threshold F_s:

$$f_T = \begin{cases} \max\left(0, 1 + \dfrac{\text{FDD} - F_s}{L_f}\right), & \text{if FDD} \leq F_s \\ 1, & \text{otherwise} \end{cases} \tag{11}$$

In addition, we assume photoperiod regulates leaf senescence as follows:

$$f_P = \begin{cases} \max\left(0, \dfrac{P - P_i}{P_x - P_i}\right), & \text{if } P \leq P_x \\ 1, & \text{otherwise} \end{cases} \tag{12}$$

where f_P is the photoperiod-limited phenology. P is day length in minutes. P_i and P_x are the lower and upper limits of day length for the period of leaf fall. Finally, the autumn phenology of DBF is determined as the product of f_T (Eq. 11) and f_P (Eq. 12). Both the spring and autumn phenology schemes have been evaluated with extensive ground records over the USA in Y2015.

3.2.2 Shrubland

Shrub phenology is sensitive to temperature and/or water availability. We calculate correlation coefficients between

Table 2. Phenological parameters for the vegetation model.

Variables	Description	Units	Value	Reference
T_b	Base temperature for budburst forcing	°C	5	Murray et al. (1989)
a	Parameters for budburst threshold G_b	Degree day	−110	Calibrated (Y2015)
b	Parameters for budburst threshold G_b	Degree day	550	Calibrated (Y2015)
r	Parameters for budburst threshold G_b	Dimensionless	−0.01	Murray et al. (1989)
L_g	Growing length	Degree day	380	Calibrated (Y2015)
T_s	Base temperature for senescence forcing	°C	20	Dufrene et al. (2005)
F_s	Threshold for leaf fall	Degree day	−140	Calibrated (Y2015)
L_f	Falling length	Degree day	410	Calibrated (Y2015)
P_x	Day length threshold for leaf fall	Minutes	695	White et al. (1997)
P_i	Day length threshold for full dormancy	Minutes	585	Calibrated (Y2015)
T_d	Threshold for drought phenology	°C	12	Calibrated (Fig. 2)
β_{min}	Lower threshold of drought limit for shrub	Dimensionless	0.4	Calibrated (Fig. S1)
β_{max}	Upper threshold of drought limit for shrub	Dimensionless	1	Calibrated (Fig. S1)
ST_b	Base soil temperature for budburst forcing	°C	0	White et al. (1997)
SG_b	Threshold for budburst with soil temperature	Degree day	100	Calibrated
SL_g	Growing length with soil temperature	Degree day	100	Calibrated
ST_s	Base soil temperature for senescence forcing	°C	10	Calibrated
SF_s	Threshold for leaf fall with soil temperature	Degree day	−80	Calibrated
SL_f	Falling length with soil temperature	Degree day	100	Calibrated
β_{min}	Lower threshold of drought limit for herbs	Dimensionless	0.3	Calibrated (Fig. S1)
β_{max}	Upper threshold of drought limit for herbs	Dimensionless	0.9	Calibrated (Fig. S1)

observed GPP and soil meteorology at 18 shrub sites (Fig. 2). For 10 sites with annual mean soil temperature $< 9\,°C$, the GPP–temperature correlations are close to 1 while the GPP–moisture correlations are all negative (Fig. 2a), suggesting that temperature is the dominant phenological driver for these plants. In contrast, for eight sites with an average soil temperature $> 14\,°C$, GPP–moisture correlations are positive and usually higher than the GPP–temperature correlations, indicating that phenology is primarily regulated by water availability at climatologically warm areas. The wide temperature gap (9–14 °C) is due to the limit in the availability of shrub sites. Here, we select a tentative threshold of 12 °C to distinguish cold and drought species. We also try to identify phenological drivers based on soil moisture thresholds but find that both temperature- and drought-dependent phenology may occur at moderately dry conditions (Fig. 2b).

In the model, we apply the temperature-dependent phenology f_T for shrubland if the site has annual mean soil temperature $< 12\,°C$. We use the same f_T as that for DBF (Eqs. 9, 11), due to the lack of long-term phenology measurements at the shrub sites. However, if the soil temperature is $> 12\,°C$, the plant growth is controlled by drought-limit phenology f_D instead:

$$f_D = \begin{cases} \max\left(0, \dfrac{\beta_{10} - \beta_{min}}{\beta_{max} - \beta_{min}}\right), & \text{if } \beta_{10} \leq \beta_{max}, \\ 1, & \text{otherwise} \end{cases} \quad (13)$$

where β_{10} is the 10-day average water stress calculated based on soil moisture, soil ice fraction, and root fraction of each soil layer (Porporato et al., 2001). The value of β_{10} changes

from 0 to 1, with a lower value indicating drier soil. Two thresholds, β_{max} and β_{min}, represent the upper and lower thresholds that trigger the drought limit for woody species. The values of these thresholds are set to $\beta_{max} = 1$ and $\beta_{min} = 0.4$ so that the predicted phenology has the maximum correlations with the observed GPP seasonality (Fig. S1a in the Supplement). The shrub phenology applies for shrubland in tropical and subtropical areas, as well as tundra at the subarctic regions, though the phenology of the latter is usually dependent on temperature alone because the climatological soil temperature is $< 12\,°C$.

3.2.3 Grassland

In the model, we consider temperature-dependent phenology for grassland based on soil temperature (ST) accumulation (White et al., 1997):

$$SGDD = \sum_{i=1}^{n} \max(ST_{10} - ST_b, 0), \quad (14)$$

where ST_{10} is the 10-day average soil temperature and $ST_b = 0\,°C$. Similar to DBF, the onset of grass greenness is triggered if soil-temperature-based growing degree day (SGDD) is higher than a threshold value SG_b (Kim et al., 2015):

$$f_T = \begin{cases} \min\left(1, \dfrac{SGDD - SG_b}{SL_g}\right), & \text{if } SGDD \geq SG_b, \\ 0, & \text{otherwise} \end{cases} \quad (15)$$

where SL_g determines the grow length of grass. Both SG_b and SL_g are calibrated based on observed GPP seasonality at FLUXNET sites (Table 2). Grass phenology at warm

sites is also sensitive to water stress (Fig. 2c). We apply the same drought-limit phenology f_D as shrubland (Eq. 13) for grassland but with calibrated thresholds $\beta_{max} = 0.9$ and $\beta_{min} = 0.3$ (Fig. S1b). Different from shrubland, whose phenology is dominated by drought when ST > 12 °C (Fig. 2a), grassland phenology is jointly affected by temperature and soil moisture (Fig. 2c). As a result, the final phenology for grassland at warm regions is the minimum of f_T and f_D.

3.2.4 Other PFTs

YIBs considers two evergreen PFTs, ENF at high latitudes and EBF in tropical areas. Observations do suggest that evergreen trees experience seasonal changes in LAI, following temperature variations and/or water availability (Doughty and Goulden, 2008; Schuster et al., 2014). However, due to the large uncertainty of evergreen phenology, we set a constant phenology factor of 1.0 for these species, following the approach adopted in other process-based vegetation models (Bonan et al., 2003; Sitch et al., 2003). We implement a parameterization for the impact of cold temperature (frost hardening) on the maximum carboxylation capacity (V_{cmax}) so as to reduce cold injury for ENF during winter (Hanninen and Kramer, 2007). EBF may experience reduced photosynthesis during the dry season through the effects of water stress on stomatal conductance (Jones et al., 2014).

Crop phenology depends on planting and harvesting dates. In YIBs, we apply a global data set of crop planting and harvesting dates (Sacks et al., 2010; Unger et al., 2013). Crop budburst occurs at the planting date and the crop continues to grow for a period of 30 days until reaching full maturity ($f = 1$). The crop leaves begin to fall 15 days prior to the harvest date, after which phenology is set to 0. A similar treatment has been adopted in the CLM (Community Land Model; Bonan et al., 2003). Thus, crop productivity but not crop phenology is sensitive to the imposed meteorological forcings.

3.3 Carbon allocation

We adopt the autotrophic respiration and carbon allocation scheme applied in the dynamic global vegetation model (DGVM) TRIFFID (Cox, 2001; Clark et al., 2011). On a daily basis, the plant LAI is updated as follows:

$$\text{LAI} = f \times \text{LAI}_b, \tag{16}$$

where f is the phenological factor, and LAI_b is the biomass-balanced (or available maximum) LAI related to tree height. LAI_b is dependent on the vegetation carbon content C_{veg}, which is the sum of carbon from leaf (C_l), root (C_r), and stem (C_w):

$$C_{veg} = C_l + C_r + C_w, \tag{17}$$

where each carbon component is a function of LAI_b:

$$C_l = \sigma_l \times \text{LAI}, \tag{18a}$$

$$C_r = \sigma_l \times \text{LAI}_b, \tag{18b}$$

$$C_w = a_{wl} \times \text{LAI}_b^{b_{wl}}. \tag{18c}$$

Here σ_l is the specific leaf carbon density. a_{wl} and b_{wl} are PFT-specified allometric parameters (Table 1). The vegetation carbon content C_{veg} is updated every 10 days based on the carbon balance of assimilation, respiration, and litter fall.

$$\frac{dC_{veg}}{dt} = (1 - \lambda) \times \text{NPP} - \Lambda_l \tag{19}$$

The NPP is the net carbon uptake:

$$\text{NPP} = \text{GPP} - R_a. \tag{20}$$

Here GPP is the total photosynthesis rate integrated over LAI. Autotrophic respiration (R_a) is split into maintenance (R_{am}) and growth respiration (R_{ag}) (Clark et al., 2011):

$$R_a = R_{am} + R_{ag}. \tag{21}$$

The maintenance respiration is calculated based on nitrogen content in leaf (N_l), root (N_r), and stem (N_w) as follows:

$$R_{am} = 0.012 R_d \left(\beta + \frac{N_r + N_w}{N_l} \right). \tag{22}$$

where R_d is the dark respiration of leaf, which is dependent on leaf temperature and is integrated over whole canopy LAI. The factor of 0.012 is the unit conversion (from $\text{mol}\,CO_2\,m^{-2}\,s^{-1}$ to $\text{kg}\,C\,m^{-2}\,s^{-1}$) and β is water stress representing soil water availability. The nitrogen contents are given by

$$N_l = n_0 \times C_l, \tag{23a}$$

$$N_r = n_{rl} \times n_0 \times C_r, \tag{23b}$$

$$N_w = n_{wl} \times n_0 \times \eta \times H \times \text{LAI}. \tag{23c}$$

Here n_0 is leaf nitrogen concentration, n_{rl} and n_{wl} are ratios of nitrogen concentrations of root and stem to leaves, η is a factor scaling live stem mass to LAI and tree height H. We adopt the same values of n_0, n_{rl}, n_{wl} and η as that of the TRIFFID model (Table 1) except that n_{rl} is set to 0.5 following observations of deciduous trees by Sugiura and Tateno (2011). The growth respiration is dependent on the residual between GPP and R_{am} based on a ratio r_g set to 0.2 for all PFTs (Knorr, 2000):

$$R_{ag} = r_g \times (\text{GPP} - R_{am}). \tag{24}$$

The λ in Eq. (19) is a partitioning coefficient determining the fraction of NPP used for spreading:

$$\lambda = \begin{cases} 1, & \text{if } \text{LAI}_b > \text{LAI}_{max} \\ \dfrac{\text{LAI}_b - \text{LAI}_{min}}{\text{LAI}_{max} - \text{LAI}_{min}}, & \text{if } \text{LAI}_{min} \leq \text{LAI}_b \leq \text{LAI}_{max}, \\ 0, & \text{if } \text{LAI}_b < \text{LAI}_{min} \end{cases}$$

$$(25)$$

where LAI_{min} and LAI_{max} are minimum and maximum LAI values for a specific PFT (Table 1). In the current model version, we turn off the fractional changes by omitting λNPP in the carbon allocation but feeding it as input for the soil respiration. The litter fall rate Λ_1 in Eq. (19) consists of contributions from leaf, root, and stem as follows:

$$\Lambda_1 = \gamma_1 \times C_1 + \gamma_r \times C_r + \gamma_w \times C_w. \qquad (26)$$

Here γ_1, γ_r, and γ_w are turnover rate (year^{-1}) for leaf, root, and stem carbon respectively. The leaf turnover rate is calculated based on the phenology change every day. The root and stem turnover rates are PFT-specific constants (Table 1), derived based on the meta-analysis by Gill and Jackson (2000) for root and Stephenson and van Mantgem (2005) for stem.

3.4 Soil respiration

The soil respiration scheme is developed based on the CASA model (Potter et al., 1993; Schaefer et al., 2008), which considers carbon flows among 12 biogeochemical pools. Three live pools, including leaf C_1, root C_r, and wood C_w, contain biomass carbon assimilated from photosynthesis. Litterfall from live pools decomposes and transits in nine dead pools, which consist of one coarse woody debris (CWD) pool, three surface pools, and five soil pools. The CWD pool is composed of dead trees and woody roots. Both surface and soil have identical pools, namely structural, metabolic, and microbial pools, which are distinguished by the content and functions. The structural pool contains lignin, the metabolic pool contains labile substrates, and the microbial pool represents microbial populations. The remaining two soil pools, the slow and passive pools, consist of organic material that decays slowly. The full list of carbon flows among different pools has been illustrated by Schaefer et al. (2008) (cf. their Fig. 1).

When carbon transfers from pool j to pool i, the carbon loss of pool j is

$$L_{j2i} = f_{j2i} k_j C_j, \qquad (27)$$

where C_j is the carbon in pool j, k_j is the total carbon loss rate of pool j, and f_{j2i} is the fraction of carbon lost from pool j transferred to pool i. The coefficient k_j is dependent on soil temperature, moisture, and texture. Meanwhile, the carbon gain of pool i is,

$$G_{j2i} = e_{j2i} \times L_{j2i} = e_{j2i} f_{j2i} k_j C_j, \qquad (28)$$

where e_{j2i} is the ratio of carbon received by pool i to the total carbon transferred from pool j. The rest of the transferred carbon is lost due to heterotrophic respiration:

$$R_{j2i} = (1 - e_{j2i}) \times L_{j2i}. \qquad (29)$$

As a result, the carbon in the ith pool is calculated as

$$\frac{dC_i}{dt} = \sum_{j=1}^{n} G_{j2i} - \sum_{k=1}^{m} L_{i2k}. \qquad (30)$$

The total heterotrophic respiration (R_h) is the summation of R_{j2i} for all pair pools where carbon transitions occur. The total soil carbon is the summation of carbon for all dead pools:

$$C_{soil} = \sum_{i=1}^{9} C_i. \qquad (31)$$

The net ecosystem productivity (NEP) is calculated as

$$NEP = -NEE = NPP - R_h = GPP - R_a - R_h, \qquad (32)$$

where NEE is the net ecosystem exchange, representing net carbon flow from land to atmosphere. YIBs does not yet account for NEE perturbations due to dynamic disturbance.

3.5 Ozone vegetation damage effects

We apply the semi-mechanistic parameterization proposed by Sitch et al. (2007) to account for ozone damage to photosynthesis through stomatal uptake. The scheme simulates associated changes in both photosynthetic rate and stomatal conductance. When photosynthesis is inhibited by ozone, stomatal conductance decreases accordingly to resist more ozone molecules. We employed an offline regional version of YIBs to show that present-day ozone damage decreases GPP by 4–8 % on average in the eastern USA and leads to larger decreases of 11–17 % in east coast hotspots (Yue and Unger, 2014). In the current model version, the photosynthesis and stomatal conductance responses to ozone damage are coupled. In future work, we will update the ozone vegetation damage function in YIBs to account for decoupled photosynthesis and stomatal conductance responses based on recent extensive metadata analyses (Wittig et al., 2007; Lombardozzi et al., 2013).

3.6 BVOC emissions

YIBs incorporates two independent leaf-level isoprene emission schemes embedded within the exact same host model framework (Zheng et al., 2015). The photosynthesis-based isoprene scheme simulates emission as a function of the electron transport-limited photosynthesis rate (J_e, Eq. 3), canopy temperature, intercellular CO_2 (c_i) and Γ_* (Arneth et al., 2007; Unger et al., 2013). The MEGAN (Model of Emissions of Gases and Aerosols from Nature) scheme applies the commonly used leaf-level functions of light and canopy temperature (Guenther et al., 1993, 1995, 2012). Both isoprene schemes account for atmospheric CO_2 sensitivity (Arneth et al., 2007). Long-term increases (decreases) in atmospheric CO_2 decrease (increase) isoprene emissions (Unger

et al., 2013). The CO_2 sensitivity is higher under lower atmospheric CO_2 levels than at present day. Leaf-level monoterpene emissions are simulated using a simplified temperature-dependent algorithm (Lathière et al., 2006). The leaf-level isoprene and monoterpene emissions are integrated over the multiple canopy layers in the exact same way as GPP to obtain the total canopy-level emissions.

3.7 Implementation of YIBs into NASA ModelE2 (NASA ModelE2-YIBs)

NASA ModelE2 has a spatial resolution of $2° \times 2.5°$ latitude by longitude with 40 vertical levels extending to 0.1 hPa. In the online configuration, the global climate model provides the meteorological drivers to YIBs and the land-surface hydrology submodel provides the soil characteristics (Rosenzweig and Abramopoulos, 1997; Schmidt et al., 2014). Recent relevant updates to NASA ModelE2 include a dynamic fire activity parameterization from Pechony and Shindell (2009) and climate-sensitive soil NO_x emissions based on Yienger and Levy (1995) (Unger and Yue, 2014). Without the YIBs implementation, the default NASA ModelE2 computes dry deposition using fixed LAI and vegetation cover fields from Olson et al. (2001), which are different from the climate model's vegetation scheme (Shindell et al., 2013b). With YIBs embedded in NASA ModelE2, the YIBs model provides the vegetation cover and LAI for the dry deposition scheme. The online-simulated atmospheric ozone and aerosol concentrations influence terrestrial carbon assimilation and stomatal conductance at the 30 min integration time step. In turn, the online vegetation properties, and water, energy and BVOC fluxes affect air quality, meteorology and the atmospheric chemical composition. The model simulates the interactive deposition of inorganic and organic nitrogen to the terrestrial biosphere. However, the YIBs biosphere currently applies fixed nitrogen levels and does not yet account for the dynamic interactions between the carbon and nitrogen cycles, and the consequences for carbon assimilation, which are highly uncertain (e.g., Thornton et al., 2007; Koven et al., 2013; Thomas et al., 2013; Zaehle et al., 2014; Houlton et al., 2015).

4 Model setup and simulations

4.1 Site-level simulations (YIBs-site)

We perform site-level simulations with the offline YIBs model at 145 eddy covariance flux tower sites for the corresponding PFTs (Fig. 1). Hourly in situ measurements of meteorology (Sect. 2.1) are used as input for the model. We gap-filled missing measurements with the Global Modeling and Assimilation Office (GMAO) Modern Era-Retrospective Analysis (MERRA) reanalysis (Rienecker et al., 2011), as described in Yue and Unger (2014). All grasslands and most croplands are considered as C3 plants, except for some

sites where corn is grown. Meteorological measurements are available for a wide range of time periods across the different sites ranging from the minimum of 1 year at some sites (e.g., BE-Jal) to the maximum of 16 years at Harvard Forest (US-HA1). The soil carbon pool initial conditions at each site are provided by the 140-year spinup procedure using YIBs-offline (Supplement). An additional 30-year spinup is conducted for each site-level simulation using the initial height H_0 for corresponding PFT (Table 1) and the fixed meteorology and CO_2 conditions at the first year of observations. Then, the simulation is continued with year-to-year forcings at the specific site for the rest of the measurement period. For all grass and shrub sites, two simulations are performed. One applies additional drought controls on phenology as described in Sects. 3.2.2 and 3.2.3, while the other uses only temperature-dependent phenology. By comparing results of these two simulations, we assess the role of drought phenology for plants in arid and semi-arid regions.

4.2 Global offline simulation (YIBs-offline)

The global offline YIBs applies the CLM land cover data set (Oleson et al., 2010). Land cover is derived based on retrievals from both MODIS (Hansen et al., 2003) and AVHRR (Defries et al., 2000). Fractions of 16 PFTs are aggregated into 9 model PFTs (Table 1). The soil carbon pool and tree height initial conditions are provided by the 140-year spinup procedure using YIBs-offline (Supplement). The global offline YIBs model is driven with WFDEI meteorology (Weedon et al., 2014) at $1° \times 1°$ horizontal resolution for the period of 1980–2011. Observed atmospheric CO_2 concentrations are adopted from the fifth assessment report (AR5) of the Intergovernmental Panel on Climate Change (IPCC; Meinshausen et al., 2011). We evaluate the simulated long-term 1980–2011 average tree height/LAI and carbon fluxes with available observations and recent multimodel intercomparisons. Attribution of the decadal trends in terrestrial carbon fluxes are explored in a separate follow-on companion study (Yue et al., 2015b).

4.3 Global online simulation in NASA ModelE2-YIBs

The global land cover data is identical to that used in YIBs-offline (Sect. 4.2) based on the CLM cover. Because our major research goal is to study short-term (seasonal, annual, decadal) interactions between vegetation physiology and atmospheric chemistry, we elect to prescribe the PFT distribution in different climatic states. We perform an online atmosphere-only simulation representative of the present day ($\sim$2000s) climatology by prescribing fixed monthly-average sea surface temperature (SST) and sea ice temperature for the 1996–2005 decade from the Hadley Center as the boundary conditions (Rayner et al., 2006). Atmospheric CO_2 concentration is fixed at the level of the year 2000 (370 ppm). In NASA ModelE2-YIBs, initial conditions for

soil carbon pools and tree heights are provided by the 140-year spinup process described in the Supplement using YIBs-offline but for year 2000 (not 1980) fixed WFDEI meteorology and atmospheric CO_2 conditions. The NASA ModelE2-YIBs global carbon–chemistry–climate model is run for an additional 30 model years. The first 20 years are discarded as the online spinup and the last 10-year results are averaged for the analyses including comparisons with observations and the YIBs-offline.

4.4 Ozone vegetation damage simulation (YIBs-ozone)

We perform two simulations to quantify ozone vegetation damage with the offline YIBs model based on the high and low ozone sensitivity parameterizations (Sitch et al., 2007). Similar to the setup in Yue and Unger (2014), we use offline hourly surface ozone concentrations simulated with the NASA ModelE2 based on the climatology and precursor emissions of the year 2000 (Sect. 4.3). In this way, atmospheric ozone photosynthesis damage affects plant growth, including changes in tree height and LAI. We compare the simulated ozone damage effects with the previous results in Yue and Unger (2014) that used prescribed LAI. For this updated assessment, we do not isolate possible feedbacks from the resultant land carbon cycle changes to the surface ozone concentrations themselves, for instance through concomitant changes to BVOC emissions and water fluxes. The importance of these feedbacks will be quantified in future research using the online NASA ModelE2-YIBs framework.

5 Results

5.1 Site-level evaluation

The simulated monthly-average GPP is compared with measurements at 145 sites for different PFTs (Fig. 3). GPP simulation biases range from -19 to 7 % depending on PFT. The highest correlation of 0.86 is achieved for DBF, mainly contributed by the reasonable phenology simulated at these sites (Fig. S2). The correlation is also high for ENF sites even though phenology is set to a constant value of 1.0. A relatively low correlation of 0.65 is modeled for EBF sites (Fig. S2). However, the site-specific evaluation shows that the simulations reasonably capture the observed magnitude and seasonality, including the minimum GPP in summer due to drought at some sites (e.g., FR-Pue and IT-Lec). Predictions at crop sites achieve a medium correlation of 0.77, because the prescribed crop phenology based on the planting and harvesting dates data set matches reality for most sites with some exceptions (e.g., CH-Oe2). Measured GPP at shrub and grass sites show varied seasonality. For most sites, the maximum carbon fluxes are measured in the hemispheric summer season. However, for sites with arid or Mediterranean climate, the summer GPP is usually the lowest during the year (e.g., ES-LMa and US-Var in Fig. S2) while the
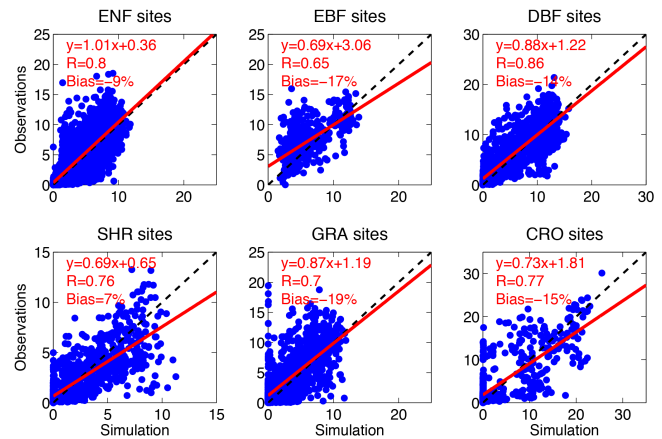

Figure 3. Comparison between observed and simulated monthly GPP (in $g\,C\,m^{-2}\,day^{-1}$) from FLUXNET and NACP networks grouped by PFTs. Each point represents the average value of 1 month at one site. The red lines indicate linear regression between observations and simulations. The regression fit, correlation coefficient, and relative bias are shown on each panel. The PFTs include evergreen needleleaf forest (ENF), evergreen broadleaf forest (EBF), deciduous broadleaf forest (DBF), shrubland (SHR), grassland (GRA), and cropland (CRO). The detailed comparison for each site is shown in Fig. S2.

peak flux is observed during the wet season when the climate is cooler and moister. Implementing the drought-dependent phenology helps improve the GPP seasonality and decrease the root-mean-square error (RMSE) at most warm climate shrub and grass sites (Fig. S3).

A synthesis of the site-level evaluation is presented in Fig. 4. Among the 145 sites, 121 have correlations higher than 0.8 for the GPP simulation (Fig. 4a). Predictions are better for PFTs with larger seasonal variations. For example, high correlations of > 0.8 are achieved at 95 % for the ENF and DBF sites, but only 70 % for grass and 45 % for EBF sites. Low relative biases (-33 to 50 %) are achieved at 94 sites (Fig. 4b). For most PFTs, a similar fraction (65 %) of the sites have low biases falling into that range, except for cropland, where only seven sites (45 %) have the low biases. The RMSE is lower than $3\,g\,[C]\,day^{-1}$ for 107 out of 145 sites (Fig. 4c). The highest RMSE is predicted for crop sites, where the model misses the large interannual variations due to crop rotation at some sites (e.g., BE-Lon, DE-Geb, and US-Ne2). The YIBs model performs simulations at the PFT level while measurements show large uncertainties in the carbon fluxes among biomes/species within the same PFT (Luyssaert et al., 2007). The simulated intraspecific variations (in the form of standard deviation) are smaller than the measured/derived values for most PFTs (Table S2), likely because of the application of fixed photosynthetic parameters for each PFT (Table 1).

Compared with GPP, the NEE simulations have smaller correlations with measurements because of the limited sea-
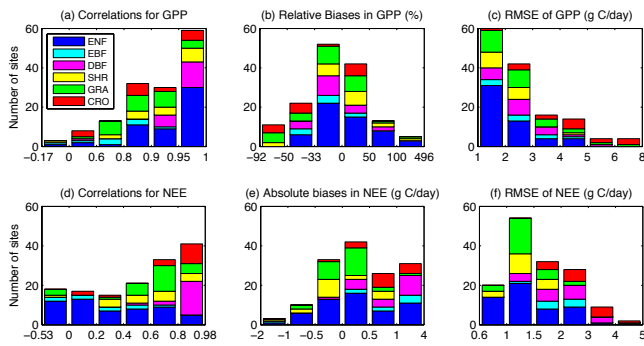
Figure 4. Bar charts of **(a, d)** correlation coefficients (R), **(b, e)** biases, and **(c, f)** RMSE for monthly **(a–c)** GPP and **(d–f)** NEE between simulations and observations at 145 sites. Each bar represents the number of sites where the R, bias, or RMSE of simulations fall between the specific ranges as defined by the x axis intervals. The minimum and maximum of each statistical metric are indicated as the two ends of the x axis in the plots. The values of the x axis are not even. The absolute biases instead of relative biases are shown for NEE because the long-term average NEE (the denominator) is usually close to zero at most sites. The PFT definitions are as in Fig. 2. Detailed comparisons at each site are shown in Figs. S2 and S4.

sonality in the observations at most sites (Fig. S4). In total, 74 sites (51 %) have correlation coefficients higher than 0.6 (Fig. 4d) and 75 sites (52 %) have absolute biases within ± 0.5 g [C] day^{-1} (Fig. 4e). For most ENF sites, the maximum net carbon uptake (the minimum NEE) is observed in spring or early summer, when GPP begins to increase while soil respiration is still at a low rate due to the cool and wet conditions (e.g., CA-Ojp and ES-ES1). Compared with other PFTs, the DBF trees usually have larger seasonality with the NEE peak in the early summer. Such seasonality helps promote correlations between model and measurements, resulting in high R (> 0.8) for 17 out of 20 sites (Fig. 4d). For shrub and grass sites, the observed seasonality of NEE is not regular, though most show maximum carbon uptake in spring or early summer. Implementation of drought-dependent phenology helps improve the simulated NEE seasonality at some sites of these PFTs (e.g., ES-LMa and IT-Pia); however, such improvement is limited for others (Fig. S4). Simulated crop NEE reaches its maximum magnitude in summer at most sites, consistent with observations, leading to a high R (> 0.8) in 10 out 16 sites (Fig. 4d). The RMSE of simulated NEE is larger for crops relative to other PFTs because the model does not treat crop rotation (Fig. 4f).

5.2 Evaluation of YIBs-offline

YIBs-offline forced with WFDEI meteorology simulates reasonable spatial distributions for tree height, LAI, and GPP, all of which show maximums in the tropical rainforest biome and medium values in the Northern Hemisphere high latitudes (Fig. 5). Compared with the satellite observations, the
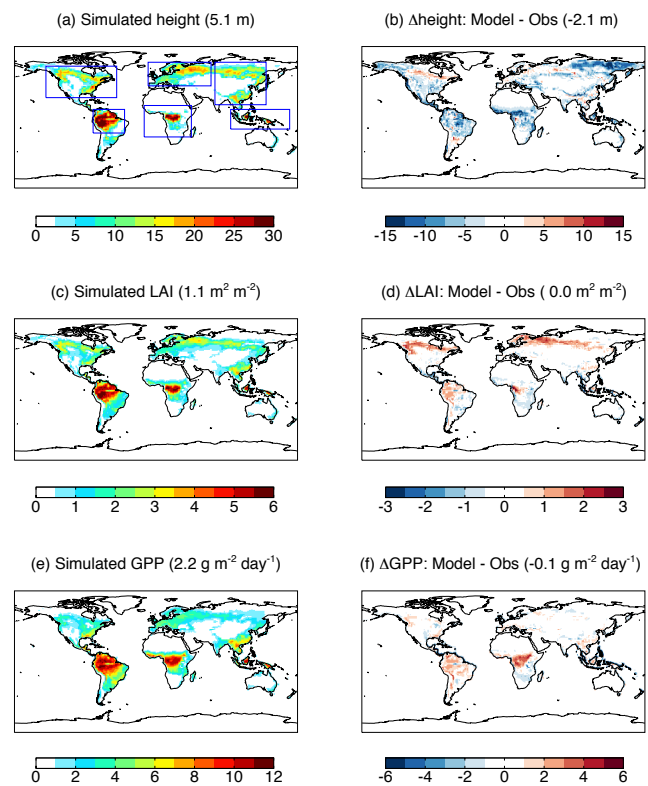

Figure 5. Simulated **(a)** tree height, **(c)** LAI, and **(e)** GPP and their differences relative to observations **(b, d, f)**. GPP data set is from Jung et al. (2009). Simulations are performed with WFDEI reanalysis. Statistics are the annual average for the period 1982–2011. The boxes in panel **(a)** represent six regions used for seasonal comparison in Fig. 6.

simulated height is underestimated by 30 % on the annual and global mean basis (Fig. 5b). Regionally, the prediction is larger by only 4 % for tropical rainforest and temperate DBF, but by 27 % for boreal ENF, for which the model assumes a constant phenology of 1.0 all the year round. However, for the vast areas covered with grass and shrub PFTs, the simulated height is lower by 41 % with maximum underestimation in eastern Siberia, where the model land is covered with short tundra. The modeled LAI is remarkably close to observations on the annual and global mean basis (Fig. 5c, d). However, there are substantial regional biases in model LAI. Model LAI prediction is higher by 0.8 m^2 m^{-2} (70 %) for boreal ENF and by 0.1 m^2 m^{-2} (5 %) for tropical rainforest. In contrast, the simulation underestimates LAI of tropical C4 grass by 0.4 m^2 m^{-2} (30 %) and shrubland by 0.2 m^2 m^{-2} (30 %). The GPP simulation is lower than the FLUXNET-derived value by 5 % on the global scale, which is contributed by the minor underestimation for all PFTs except for tropical rainforest, where model predicts 9 % higher GPP than observations (Fig. 5f).

The model simulates reasonable seasonality for LAI and land carbon fluxes (Fig. 6). Tree height shows limited sea-
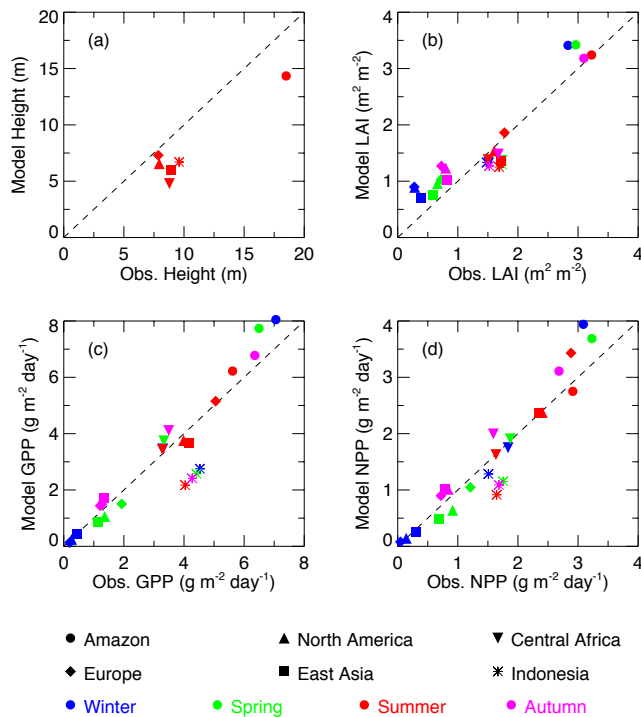
Figure 6. Comparison of annual (**a**) tree height and seasonal (**b**) LAI, (**c**) GPP, and (**d**) (NPP between simulations and observations for the six regions shown in Fig. 5a. GPP data set is from Jung et al. (2009). Values at different regions are marked using different symbols, with distinct colors indicating seasonal means for winter (blue, December–February), spring (green, March–May), summer (red, June–August), and autumn (magenta, September–November).

Figure 7. Comparison of simulated global GPP and net biome productivity (NBP) from (red) YIBs-offline and (blue) ModelE2-YIBs models with 10 other carbon cycle models for 1982–2008. Each black symbol represents an independent model as summarized in Piao et al. (2013). Error bars indicate the standard deviations for interannual variability. The gray shading represents the global residual land sink (RLS) calculated in Friedlingstein et al. (2010). The green line at the top represents the range of GPP for 1982–2008 estimated by Jung et al. (2011) and the magenta line represents GPP for 1982–2011 from Jung et al. (2009).

sonal variations, especially for DBF, ENF, and EBF trees. LAI, GPP, and NPP also exhibit small seasonality over tropical areas, such as the Amazon, central Africa, and Indonesia. However, for temperate areas, such as North America, Europe and east Asia, these variables show large seasonal variations with a minimum in winter and maximum in summer. The LAI is overestimated by 20 % in the Amazon during the December-January-February season but underestimated by 25 % in Indonesia during summer (Fig. 6b). For GPP and NPP, the positive bias in Indonesia is even larger at 45 % during summer (Fig. 6c, d).

On the global scale, YIBs-offline simulates a GPP of $124.6 \pm 3.3\,\mathrm{Pg\,C\,a^{-1}}$ and NEE of $-2.5 \pm 0.7\,\mathrm{Pg\,C\,a^{-1}}$ for 1982–2011. These values are consistent with estimates upscaled from the FLUXNET observations (Jung et al., 2009, 2011; Friedlingstein et al., 2010) and simulations from 10 other carbon cycle models (Piao et al., 2013) (Fig. 7). The net biome productivity (NBP) is in opposite sign to NEE. Tropical areas (23° S–23° N) account for 63 % of the global GPP, including 27 % from the Amazon rainforest, 21 % from central Africa, and 5 % from Indonesia forest (Table 3). A lower contribution of 57 % from the tropics is predicted for both NPP and heterotrophic respiration. However, for NEE,
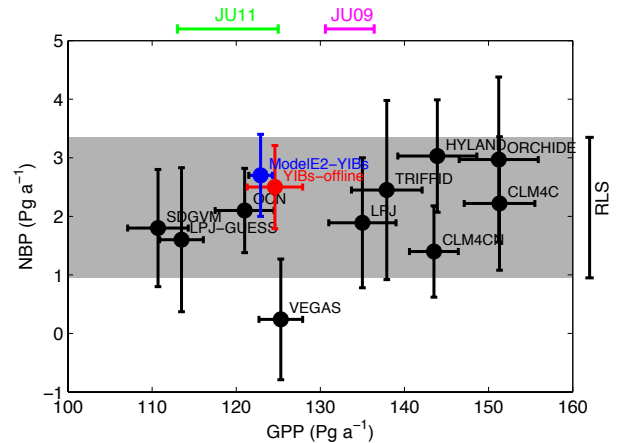
only 40 % of the land carbon sink is contributed by tropical forests and grasslands, while 56 % is from temperate forests and grasslands in North America, Europe, and east Asia.

We compare the simulated budburst dates with observations from satellite retrieval (Fig. 8). The model captures the basic spatial pattern of spring phenology with earlier to later budburst dates from lower to higher latitudes. On average, the observed budburst date in the Northern Hemisphere is DOY 133 (13 May) and the simulated is DOY 132 (12 May). Such close estimate results from the regional delay of 10 days (DOY 119 vs. 129) in Europe and advance of 4 days (DOY 140 vs. 136) in east Asia. In Y2015, extensive (∼ 75 000 records) ground-based measurements have been used to validate the simulated spring and autumn phenology in the USA and both the spatial distribution and interannual variation of the simulation are reasonable.

5.3 Evaluation of NASA ModelE2-YIBs

NASA ModelE2-YIBs simulations of global land carbon fluxes show similar spatial distribution and magnitude as the YIBs-offline model (Figs. S6–S8). However, due to differences in the meteorological forcings (Figs. S9–S12), regional discrepancies between the two configurations occur. The predicted LAI with NASA ModelE2-YIBs is lower by 20 % in the Amazon region than with YIBs-offline (Fig. S6), following the similar magnitude of differences in regional GPP and NPP (Figs. S7, S8). We performed driver attribution sensitivity simulations in which the YIBs-offline con-

Table 3. Summary of carbon fluxes and ozone vegetation damage in different domains and for the tropics (23° S–23° N).

Regions	Amazon	North America	Central Africa	Europe	East Asia	Indonesia	Tropics	Global
GPP (Pg C a^{-1})	33.4	12.3	25.7	11.5	17.9	6.7	77.9	124.6
NPP (Pg C a^{-1})	15.5	7.5	12.1	7.3	10.3	2.9	36.8	65
NEE (Pg C a^{-1})	−0.4	−0.5	−0.3	−0.4	−0.5	−0.1	−1.0	−2.5
Ra (Pg C a^{-1})	17.9	4.8	13.6	4.2	7.6	3.8	41.1	59.6
Rh (Pg C a^{-1})	15.1	7	11.8	6.9	9.8	2.8	35.8	62.5
Low ozone damage to GPP (%)	−0.9	−2.4	−1.8	−2.5	−4.3	−3	−1.7	−2.1
High ozone damage to GPP (%)	−2.6	−5.8	−4.4	−6.1	−9.6	−7.3	−4.4	−5
Low ozone damage to LAI (%)	−0.3	−0.5	−0.6	−0.5	−0.9	−0.8	−0.5	−0.5
High ozone damage to LAI (%)	−0.8	−1.2	−1.6	−1.4	−2.4	−2.1	−1.4	−1.4

(a) Average greenness onset date from satellite

(b) Predictd average budburst date

60   80   100   120   140   160   180   200   (DOY)

(c) Differences: prediction − observation

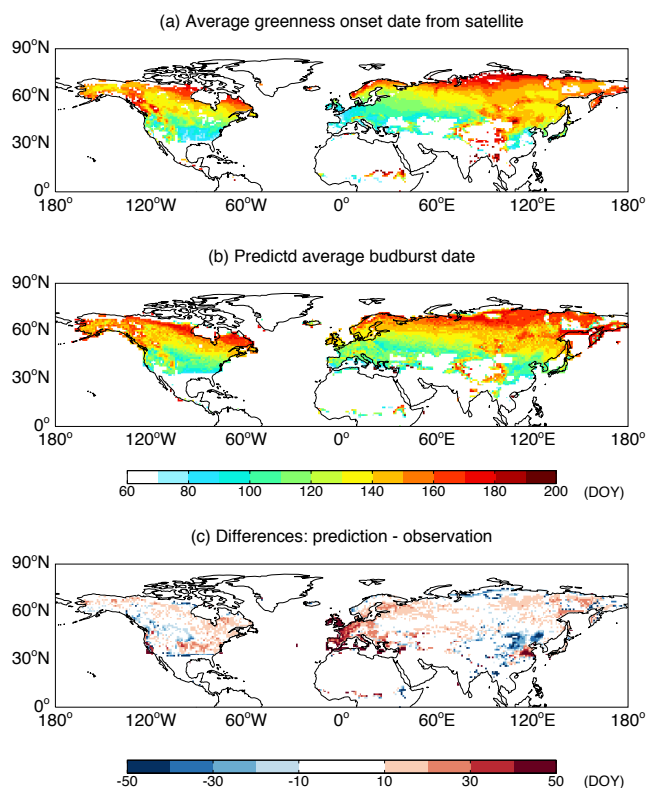-50   -30   -10   10   30   50   (DOY)

Figure 8. Comparison of simulated budburst dates in the Northern Hemisphere with remote sensing. Simulated phenology in each grid square is the composite result from DBF, tundra, shrubland, and grassland based on PFT fraction and LAI in that grid box. Both simulations and observations are averaged for the period 1982–2011. Results for the Southern Hemisphere are not shown due to the limited coverage of deciduous forests and cold grass species.

figuration is driven with the same meteorological forcings simulated by NASA ModelE2 except for one selected field from the WFDEI reanalysis. We found that the anomalously warmer climate over the Amazon in the global climate model (Fig. S9) causes the lower GPP in that region in NASA ModelE2-YIBs. The temperature optimum for C3 photosynthesis is around 30 °C, above which the maximum rate of

electron transport (Eq. 3) decreases dramatically (Farquhar et al., 1980). As a result, the higher NASA ModelE2-YIBs surface temperature in the tropical rainforest results in the lower photosynthesis rates there. With the exception of the Amazon, the NASA ModelE2-YIBs June-July-August GPP and NPP show low biases in central Africa and high latitudes in North America and Asia but high biases in Europe, western USA, and eastern China (Figs. S7, S8). The sensitivity tests attribute these discrepancies to differences in canopy humidity (Fig. S11) and soil wetness (Fig. S12). Low soil wetness decreases water stress β, reduces the slope m of the Ball–Berry equation (Eq. 6), and consequently limits photosynthesis by declining stomatal conductance in combination with low humidity. On the global scale, the ModelE2-YIBs simulates annual GPP of 122.9 Pg C, NPP of 62 Pg C, and NEE of −2.7 Pg C, all of which are close to the YIBs-offline simulation (Table 3) and consistent with results from observations and model intercomparison (Fig. 7).

5.4 Assessment of global ozone vegetation damage

Ozone dampens GPP and consequently affects tree growth and LAI. In North America, the annual average reductions range from 2 to 6 %, depending on the plant sensitivity to ozone damage (Table 3). Locally, average damages reach as high as 5–11 % in the eastern USA with maximums up to 11–23 % (Fig. 9a, b). These values are higher than the estimate of 4–8 % (maximum 11–17 %) by Yue and Unger (2014) because the latter used prescribed LAI in the simulation and did not consider the LAI reductions due to ozone damage (Fig. 9c, d). The YIBs model predicts a similar magnitude of damages in Europe compared to North America but almost doubled its effects in east Asia (Table 3) due to the high ozone concentrations there, especially in boreal summer (Fig. S5). Ozone-induced GPP reductions are limited in tropical areas (Fig. 5e) because the surface ozone levels there are very low, for example, especially over the Amazon forest (Fig. S5). The damage to LAI generally follows the pattern of GPP reductions but the response signal is weaker than that of GPP (Fig. 9c, d).
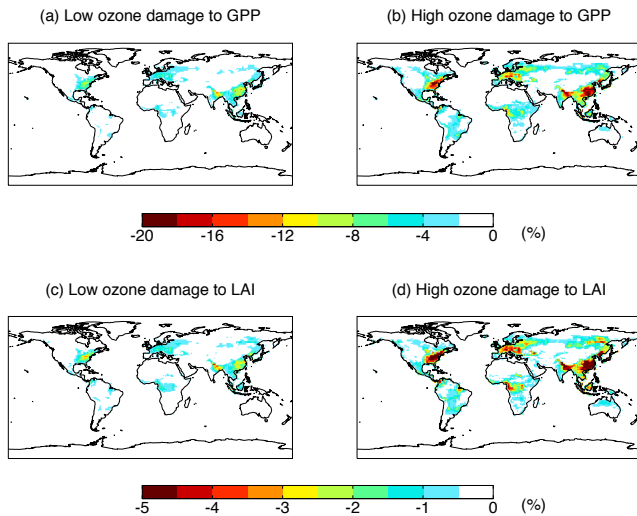
Figure 9. Percentage of ozone vegetation damage to (top) GPP and (bottom) LAI with **(a, c)** low and **(b, d)** high sensitivity. Both damages of GPP and LAI are averaged for 1982–2011. Offline surface ozone concentrations (Fig. S5) are simulated by the GISS ModelE2 with climatology of the year 2000.

6 Conclusions and discussion

We describe and evaluate the process-based YIBs interactive terrestrial biosphere model. YIBs is embedded into the NASA ModelE2 global chemistry–climate model and is an important urgently needed development to improve the biological realism of interactions between vegetation, atmospheric chemistry and climate. We implement both temperature- and drought-dependent phenology for DBF, shrub, and grass species. The model simulates interactive ozone vegetation damage. The YIBs model is fully validated with land carbon flux measurements from 145 ground stations and global observations of canopy height, LAI, GPP, NPP, and phenology from multiple satellite retrievals.

There are several limitations in the current model setup. The vegetation parameters, V_{cmax25}, m, and b (Table 1) are fixed at the PFT level, which may induce uncertainties in the simulation of carbon fluxes due to intraspecific variations (Kattge et al., 2011). The model does not yet include a dynamic treatment of nitrogen and phosphorous availability because current schemes suffer from large uncertainties (Thornton et al., 2007; Zaehle et al., 2014; Houlton et al., 2015). Phenology is set to a constant value of 1 for ENF and EBF, which is not consistent with observations (O'Keefe, 2000; Jones et al., 2014). The ozone damage scheme of Sitch et al. (2007) considers coupled responses of photosynthesis and stomatal conductance while observations suggest a decoupling (Lombardozzi et al., 2013).

Despite these limitations, the YIBs model reasonably simulates global land carbon fluxes compared with both site-level flux measurements and global satellite observations.

YIBs is primed for ongoing development, for example, incorporating community dynamics including mortality, establishment, seed transport and dynamic fire disturbance (Moorcroft et al., 2001). NASA ModelE2-YIBs is available to be integrated with interactive ocean and atmospheric carbon components to offer a full global carbon–climate model, for example, for use in interpreting and diagnosing new satellite data sets of atmospheric CO_2 concentrations. In the current form, NASA ModelE2-YIBs provides a useful new tool to investigate the impacts of air pollution on the carbon budget, water cycle, and surface energy balance, and, in turn, the impacts of changing vegetation physiology on the atmospheric chemical composition. Carbon–chemistry–climate interactions, a relatively new interdisciplinary research frontier, are expected to influence the evolution of Earth's climate system on multiple spatiotemporal scales.

Code availability

The YIBs model (version 1.0) site-level source code is available at https://github.com/YIBS01/YIBS_site. The source codes for the global offline and global online versions of the YIBs model (version 1.0) are available through collaboration. Please submit a request to X. Yue (xu.yue@yale.edu) and N. Unger (nadine.unger@yale.edu). Auxiliary forcing data and related input files must be obtained independently.

The Supplement related to this article is available online at doi:10.5194/gmd-8-2399-2015-supplement.

References

Ainsworth, E. A., Yendrek, C. R., Sitch, S., Collins, W. J., and Emberson, L. D.: The effects of tropospheric ozone on net primary productivity and implications for climate change, Annu. Rev. Plant Biol., 63, 637–661, doi:10.1146/Annurev-Arplant-042110-103829, 2012.

Arneth, A., Niinemets, Ü., Pressley, S., Bäck, J., Hari, P., Karl, T., Noe, S., Prentice, I. C., Serça, D., Hickler, T., Wolf, A., and Smith, B.: Process-based estimates of terrestrial ecosystem isoprene emissions: incorporating the effects of a direct CO_2-isoprene interaction, Atmos. Chem. Phys., 7, 31–53, doi:10.5194/acp-7-31-2007, 2007.

Baldocchi, D.: An Analytical Solution for Coupled Leaf Photosynthesis and Stomatal Conductance Models, Tree Physiol., 14, 1069–1079, 1994.

Ball, J. T., Woodrow, I. E., and Berry, J. A.: A model predicting stomatal conductance and its contribution to the control of photosynthesis under different environmental conditions, in: Progress in Photosynthesis Research, edited by: Biggins, J., Nijhoff, Dordrecht, the Netherlands, 221–224, 1987.

Beer, C., Reichstein, M., Tomelleri, E., Ciais, P., Jung, M., Carvalhais, N., Rodenbeck, C., Arain, M. A., Baldocchi, D., Bonan, G. B., Bondeau, A., Cescatti, A., Lasslop, G., Lindroth, A., Lomas, M., Luyssaert, S., Margolis, H., Oleson, K. W., Roupsard, O., Veenendaal, E., Viovy, N., Williams, C., Woodward, F. I., and Papale, D.: Terrestrial Gross Carbon Dioxide Uptake: Global Distribution and Covariation with Climate, Science, 329, 834–838, doi:10.1126/Science.1184984, 2010.

Berry, J. A., Beerling, D. J., and Franks, P. J.: Stomata: key players in the earth system, past and present, Curr. Opin. Plant Biol., 13, 233–240, doi:10.1016/J.Pbi.2010.04.013, 2010.

Bonan, G. B., Levis, S., Sitch, S., Vertenstein, M., and Oleson, K. W.: A dynamic global vegetation model for use with climate models: concepts and description of simulated vegetation dynamics, Glob. Change Biol., 9, 1543–1566, doi:10.1046/J.1365-2486.2003.00681.X, 2003.

Bonan, G. B., Lawrence, P. J., Oleson, K. W., Levis, S., Jung, M., Reichstein, M., Lawrence, D. M., and Swenson, S. C.: Improving canopy processes in the Community Land Model version 4 (CLM4) using global flux fields empirically inferred from FLUXNET data, J. Geophys. Res., 116, G02014, doi:10.1029/2010jg001593, 2011.

Clark, D. B., Mercado, L. M., Sitch, S., Jones, C. D., Gedney, N., Best, M. J., Pryor, M., Rooney, G. G., Essery, R. L. H., Blyth, E., Boucher, O., Harding, R. J., Huntingford, C., and Cox, P. M.: The Joint UK Land Environment Simulator (JULES), model description – Part 2: Carbon fluxes and vegetation dynamics, Geosci. Model Dev., 4, 701–722, doi:10.5194/gmd-4-701-2011, 2011.

Collatz, G. J., Ball, J. T., Grivet, C., and Berry, J. A.: Physiological and Environmental-Regulation of Stomatal Conductance, Photosynthesis and Transpiration – a Model That Includes a Laminar Boundary-Layer, Agr. Forest Meteorol., 54, 107–136, doi:10.1016/0168-1923(91)90002-8, 1991.

Collatz, G. J., Ribas-Carbo, M., and Berry, J. A.: Coupled Photosynthesis-Stomatal Conductance Model for Leaves of C4 Plants, Aust. J. Plant Physiol., 19, 519–538, 1992.

Cox, P. M.: Description of the "TRIFFID" Dynamic Global Vegetation Model, Hadley Centre, Technical Note 24, Berks, UK, 2001.

Defries, R. S., Hansen, M. C., Townshend, J. R. G., Janetos, A. C., and Loveland, T. R.: A new global 1-km dataset of percentage tree cover derived from remote sensing, Glob. Change Biol., 6, 247–254, doi:10.1046/J.1365-2486.2000.00296.X, 2000.

Delbart, N. and Picard, G.: Modeling the date of leaf appearance in low-arctic tundra, Glob. Change Biol., 13, 2551–2562, doi:10.1111/J.1365-2486.2007.01466.X, 2007.

Delpierre, N., Dufrene, E., Soudani, K., Ulrich, E., Cecchini, S., Boe, J., and Francois, C.: Modelling interannual and spatial variability of leaf senescence for three deciduous tree species in France, Agr. Forest Meteorol., 149, 938–948, doi:10.1016/J.Agrformet.2008.11.014, 2009.

Doughty, C. E. and Goulden, M. L.: Seasonal patterns of tropical forest leaf area index and CO_2 exchange, J. Geophys. Res., 113, G00b06, doi:10.1029/2007jg000590, 2008.

Dufrene, E., Davi, H., Francois, C., le Maire, G., Le Dantec, V., and Granier, A.: Modelling carbon and water cycles in a beech forest Part I: Model description and uncertainty analysis on modelled NEE, Ecol. Model, 185, 407–436, doi:10.1016/J.Ecolmodel.2005.01.004, 2005.

Farquhar, G. D., Caemmerer, S. V., and Berry, J. A.: A Biochemical-Model of Photosynthetic $Co2$ Assimilation in Leaves of C-3 Species, Planta, 149, 78–90, doi:10.1007/Bf00386231, 1980.

Friedlingstein, P., Cox, P., Betts, R., Bopp, L., Von Bloh, W., Brovkin, V., Cadule, P., Doney, S., Eby, M., Fung, I., Bala, G., John, J., Jones, C., Joos, F., Kato, T., Kawamiya, M., Knorr, W., Lindsay, K., Matthews, H. D., Raddatz, T., Rayner, P., Reick, C., Roeckner, E., Schnitzler, K. G., Schnur, R., Strassmann, K., Weaver, A. J., Yoshikawa, C., and Zeng, N.: Climate-carbon cycle feedback analysis: Results from the (CMIP)-M-4 model intercomparison, J. Climate, 19, 3337–3353, doi:10.1175/Jcli3800.1, 2006.

Friedlingstein, P., Houghton, R. A., Marland, G., Hackler, J., Boden, T. A., Conway, T. J., Canadell, J. G., Raupach, M. R., Ciais, P., and Le Quere, C.: Update on CO2 emissions, Nat. Geosci., 3, 811–812, doi:10.1038/Ngeo1022, 2010.

Friedlingstein, P., Andrew, R. M., Rogelj, J., Peters, G. P., Canadell, J. G., Knutti, R., Luderer, G., Raupach, M. R., Schaeffer, M., van Vuuren, D. P., and Le Quere, C.: Persistent growth of CO2 emissions and implications for reaching climate targets, Nat. Geosci., 7, 709–715, doi:10.1038/Ngeo2248, 2014.

Friend, A. D. and Kiang, N. Y.: Land surface model development for the GISS GCM: Effects of improved canopy physiology on simulated climate, J. Climate, 18, 2883–2902, doi:10.1175/Jcli3425.1, 2005.

Gill, R. A. and Jackson, R. B.: Global patterns of root turnover for terrestrial ecosystems, New Phytol., 147, 13–31, doi:10.1046/J.1469-8137.2000.00681.X, 2000.

Guenther, A. B., Zimmerman, P. R., Harley, P. C., Monson, R. K., and Fall, R.: Isoprene and Monoterpene Emission Rate Variability – Model Evaluations and Sensitivity Analyses, J. Geophys. Res., 98, 12609–12617, doi:10.1029/93jd00527, 1993.

Guenther, A. B., Hewitt, C. N., Erickson, D., Fall, R., Geron, C., Graedel, T., Harley, P., Klinger, L., Lerdau, M., Mckay, W. A., Pierce, T., Scholes, B., Steinbrecher, R., Tallamraju, R., Taylor, J., and Zimmerman, P.: A Global-Model of Natural Volatile Organic-Compound Emissions, J. Geophys. Res., 100, 8873–8892, doi:10.1029/94jd02950, 1995.

Guenther, A. B., Jiang, X., Heald, C. L., Sakulyanontvittaya, T., Duhl, T., Emmons, L. K., and Wang, X.: The Model of Emissions of Gases and Aerosols from Nature version 2.1 (MEGAN2.1): an extended and updated framework for modeling biogenic emissions, Geosci. Model Dev., 5, 1471–1492, doi:10.5194/gmd-5-1471-2012, 2012.

Hanninen, H. and Kramer, K.: A framework for modelling the annual cycle of trees in boreal and temperate regions, Silva Fenn., 41, 167–205, 2007.

Hansen, M. C., DeFries, R. S., Townshend, J. R. G., Carroll, M., Dimiceli, C., and Sohlberg, R. A.: Global Percent Tree Cover at a Spatial Resolution of 500 Meters: First Results of the MODIS Vegetation Continuous

Fields Algorithm, Earth Interact, 7, 1–15, doi:10.1175/1087-3562(2003)007<0001:GPTCAA>2.0.CO;2, 2003.

Hollaway, M. J., Arnold, S. R., Challinor, A. J., and Emberson, L. D.: Intercontinental trans-boundary contributions to ozone-induced crop yield losses in the Northern Hemisphere, Biogeosciences, 9, 271–292, doi:10.5194/bg-9-271-2012, 2012.

Houghton, R. A., House, J. I., Pongratz, J., van der Werf, G. R., De-Fries, R. S., Hansen, M. C., Le Quéré, C., and Ramankutty, N.: Carbon emissions from land use and land-cover change, Biogeosciences, 9, 5125–5142, doi:10.5194/bg-9-5125-2012, 2012.

Houlton, B. Z., Marklein, A. R., and Bai, E.: Representation of nitrogen in climate change forecasts, Nat. Clim. Change, 5, 398–401, 2015.

Huntingford, C., Cox, P. M., Mercado, L. M., Sitch, S., Bellouin, N., Boucher, O., and Gedney, N.: Highly contrasting effects of different climate forcing agents on terrestrial ecosystem services, Philos. T. R. Soc. A, 369, 2026–2037, doi:10.1098/Rsta.2010.0314, 2011.

Jones, M. O., Kimball, J. S., and Nemani, R. R.: Asynchronous Amazon forest canopy phenology indicates adaptation to both water and light availability, Environ. Res. Lett., 9, 124021, doi:10.1088/1748-9326/9/12/124021, 2014.

Jung, M., Reichstein, M., and Bondeau, A.: Towards global empirical upscaling of FLUXNET eddy covariance observations: validation of a model tree ensemble approach using a biosphere model, Biogeosciences, 6, 2001–2013, doi:10.5194/bg-6-2001-2009, 2009.

Jung, M., Reichstein, M., Margolis, H. A., Cescatti, A., Richardson, A. D., Arain, M. A., Arneth, A., Bernhofer, C., Bonal, D., Chen, J. Q., Gianelle, D., Gobron, N., Kiely, G., Kutsch, W., Lasslop, G., Law, B. E., Lindroth, A., Merbold, L., Montagnani, L., Moors, E. J., Papale, D., Sottocornola, M., Vaccari, F., and Williams, C.: Global patterns of land-atmosphere fluxes of carbon dioxide, latent heat, and sensible heat derived from eddy covariance, satellite, and meteorological observations, J. Geophys. Res., 116, G00j07, doi:10.1029/2010jg001566, 2011.

Kattge, J., Diaz, S., Lavorel, S., et al.: TRY – a global database of plant traits, Glob. Change Biol., 17, 2905–2935, doi:10.1111/J.1365-2486.2011.02451.X, 2011.

Keenan, T. F., Gray, J., Friedl, M. A., Toomey, M., Bohrer, G., Hollinger, D. Y., Munger, J. W., O'Keefe, J., Schmid, H. P., SueWing, I., Yang, B., and Richardson, A. D.: Net carbon uptake has increased through warming-induced changes in temperate forest phenology, Nat. Clim. Change, 4, 598–604, doi:10.1038/Nclimate2253, 2014.

Kim, Y., Moorcroft, P. R., Aleinov, I., Puma, M. J., and Kiang, N. Y.: Variability of phenology and fluxes of water and carbon with observed and simulated soil moisture in the Ent Terrestrial Biosphere Model (Ent TBM version 1.0.1.0.0), Geosci. Model Dev. Discuss., 8, 5809–5871, doi:10.5194/gmdd-8-5809-2015, 2015.

Knorr, W.: Annual and interannual CO_2 exchanges of the terrestrial biosphere: process-based simulations and uncertainties, Global Ecol. Biogeogr., 9, 225–252, doi:10.1046/J.1365-2699.2000.00159.X, 2000.

Koch, D., Bauer, S. E., Del Genio, A., Faluvegi, G., McConnell, J. R., Menon, S., Miller, R. L., Rind, D., Ruedy, R., Schmidt, G. A., and Shindell, D.: Coupled Aerosol-Chemistry-Climate Twentieth-Century Transient Model Investigation: Trends in

Short-Lived Species and Climate Responses, J. Climate, 24, 2693–2714, doi:10.1175/2011jcli3582.1, 2011.

Koven, C. D., Riley, W. J., Subin, Z. M., Tang, J. Y., Torn, M. S., Collins, W. D., Bonan, G. B., Lawrence, D. M., and Swenson, S. C.: The effect of vertically resolved soil biogeochemistry and alternate soil C and N models on C dynamics of CLM4, Biogeosciences, 10, 7109–7131, doi:10.5194/bg-10-7109-2013, 2013.

Lamarque, J.-F., Shindell, D. T., Josse, B., Young, P. J., Cionni, I., Eyring, V., Bergmann, D., Cameron-Smith, P., Collins, W. J., Doherty, R., Dalsoren, S., Faluvegi, G., Folberth, G., Ghan, S. J., Horowitz, L. W., Lee, Y. H., MacKenzie, I. A., Nagashima, T., Naik, V., Plummer, D., Righi, M., Rumbold, S. T., Schulz, M., Skeie, R. B., Stevenson, D. S., Strode, S., Sudo, K., Szopa, S., Voulgarakis, A., and Zeng, G.: The Atmospheric Chemistry and Climate Model Intercomparison Project (ACCMIP): overview and description of models, simulations and climate diagnostics, Geosci. Model Dev., 6, 179–206, doi:10.5194/gmd-6-179-2013, 2013.

Lathière, J., Hauglustaine, D. A., Friend, A. D., De Noblet-Ducoudré, N., Viovy, N., and Folberth, G. A.: Impact of climate variability and land use changes on global biogenic volatile organic compound emissions, Atmos. Chem. Phys., 6, 2129–2146, doi:10.5194/acp-6-2129-2006, 2006.

Liu, H., Tian, F., Hu, H. C., Hu, H. P., and Sivapalan, M.: Soil moisture controls on patterns of grass green-up in Inner Mongolia: an index based approach, Hydrol. Earth Syst. Sci., 17, 805–815, doi:10.5194/hess-17-805-2013, 2013.

Lombardozzi, D., Sparks, J. P., and Bonan, G.: Integrating O_3 influences on terrestrial processes: photosynthetic and stomatal response data available for regional and global modeling, Biogeosciences, 10, 6815–6831, doi:10.5194/bg-10-6815-2013, 2013.

Luyssaert, S., Inglima, I., Jung, M., et al.: CO_2 balance of boreal, temperate, and tropical forests derived from a global database, Glob. Change Biol., 13, 2509–2537, doi:10.1111/J.1365-2486.2007.01439.X, 2007.

Mahowald, N.: Aerosol Indirect Effect on Biogeochemical Cycles and Climate, Science, 334, 794–796, doi:10.1126/Science.1207374, 2011.

Medlyn, B. E., Duursma, R. A., Eamus, D., Ellsworth, D. S., Prentice, I. C., Barton, C. V. M., Crous, K. Y., de Angelis, P., Freeman, M., and Wingate, L.: Reconciling the optimal and empirical approaches to modelling stomatal conductance, Glob. Change Biol., 17, 2134–2144, doi:10.1111/J.1365-2486.2010.02375.X, 2011.

Meinshausen, M., Smith, S. J., Calvin, K., Daniel, J. S., Kainuma, M. L. T., Lamarque, J. F., Matsumoto, K., Montzka, S. A., Raper, S. C. B., Riahi, K., Thomson, A., Velders, G. J. M., and van Vuuren, D. P. P.: The RCP greenhouse gas concentrations and their extensions from 1765 to 2300, Climatic Change, 109, 213–241, doi:10.1007/S10584-011-0156-Z, 2011.

Mercado, L. M., Bellouin, N., Sitch, S., Boucher, O., Huntingford, C., Wild, M., and Cox, P. M.: Impact of changes in diffuse radiation on the global land carbon sink, Nature, 458, 1014–1017, doi:10.1038/Nature07949, 2009.

Miller, R. L., Schmidt, G. A., Nazarenko, L. S., Tausnev, N., Bauer, S. E., DelGenio, A. D., Kelley, M., Lo, K. K., Ruedy, R., Shindell, D. T., Aleinov, I., Bauer, M., Bleck, R., Canuto, V., Chen, Y. H., Cheng, Y., Clune, T. L., Faluvegi, G., Hansen, J. E., Healy, R. J., Kiang, N. Y., Koch, D., Lacis, A. A., LeGrande, A. N.,

Lerner, J., Menon, S., Oinas, V., Garcia-Pando, C. P., Perlwitz, J. P., Puma, M. J., Rind, D., Romanou, A., Russell, G. L., Sato, M., Sun, S., Tsigaridis, K., Unger, N., Voulgarakis, A., Yao, M. S., and Zhang, J. L.: CMIP5 historical simulations (1850–2012) with GISS ModelE2, J. Adv. Model Earth Sy., 6, 441–477, doi:10.1002/2013ms000266, 2014.

Moorcroft, P. R., Hurtt, G. C., and Pacala, S. W.: A method for scaling vegetation dynamics: The ecosystem demography model (ED), Ecol. Monogr., 71, 557–585, doi:10.1890/0012-9615(2001)071[0557:Amfsvd]2.0.Co;2, 2001.

Murray, M. B., Cannell, M. G. R., and Smith, R. I.: Date of Budburst of fifteen Tree Species in Britain Following Climatic Warming, J. Appl. Ecol., 26, 693–700, doi:10.2307/2404093, 1989.

O'Keefe, J.: Phenology of Woody Species at Harvard Forest since 1990, Long Term Ecological Research Network, doi:10.6073/pasta/b151c3eb552433a2a94c6f8de489740b, 2000.

Oleson, K. W., Lawrence, D. M., Bonan, G. B., Flanne, M. G., Kluzek, E., Lawrence, P. J., Levis, S., Swenson, S. C., and Thornton, P. E.: Technical Description of version 4.0 of the Community Land Model (CLM), National Center for Atmospheric Research, Boulder, USA, CONCAR/TN-478+STR, 2010.

Olson, D. M., Dinerstein, E., Wikramanayake, E. D., Burgess, N. D., Powell, G. V. N., Underwood, E. C., D'amico, J. A., Itoua, I., Strand, H. E., Morrison, J. C., Loucks, C. J., Allnutt, T. F., Ricketts, T. H., Kura, Y., Lamoreux, J. F., Wettengel, W. W., Hedao, P., and Kassem, K. R.: Terrestrial Ecoregions of the World: A New Map of Life on Earth, Bioscience, 51, 933–938, doi:10.1641/0006-3568(2001)051[0933:TEOTWA]2.0.CO;2, 2001.

Pechony, O. and Shindell, D. T.: Fire parameterization on a global scale, J. Geophys. Res., 114, D16115, doi:10.1029/2009jd011927, 2009.

Piao, S. L., Sitch, S., Ciais, P., Friedlingstein, P., Peylin, P., Wang, X. H., Ahlstrom, A., Anav, A., Canadell, J. G., Cong, N., Huntingford, C., Jung, M., Levis, S., Levy, P. E., Li, J. S., Lin, X., Lomas, M. R., Lu, M., Luo, Y. Q., Ma, Y. C., Myneni, R. B., Poulter, B., Sun, Z. Z., Wang, T., Viovy, N., Zaehle, S., and Zeng, N.: Evaluation of terrestrial carbon cycle models for their response to climate variability and to CO_2 trends, Glob. Change Biol., 19, 2117–2132, doi:10.1111/Gcb.12187, 2013.

Pieruschka, R., Huber, G., and Berry, J. A.: Control of transpiration by radiation, P. Natl. Acad. Sci. USA, 107, 13372–13377, doi:10.1073/Pnas.0913177107, 2010.

Porporato, A., Laio, F., Ridolfi, L., and Rodriguez-Iturbe, I.: Plants in water-controlled ecosystems: active role in hydrologic processes and response to water stress – III. Vegetation water stress, Adv. Water Resour., 24, 725–744, doi:10.1016/S0309-1708(01)00006-9, 2001.

Potter, C. S., Randerson, J. T., Field, C. B., Matson, P. A., Vitousek, P. M., Mooney, H. A., and Klooster, S. A.: Terrestrial Ecosystem Production – a Process Model-Based on Global Satellite and Surface Data, Global Biogeochem. Cy., 7, 811–841, doi:10.1029/93gb02725, 1993.

Rayner, N. A., Brohan, P., Parker, D. E., Folland, C. K., Kennedy, J. J., Vanicek, M., Ansell, T. J., and Tett, S. F. B.: Improved analyses of changes and uncertainties in sea surface temperature measured in situ sice the mid-nineteenth century: The HadSST2 dataset, J. Climate, 19, 446–469, doi:10.1175/Jcli3637.1, 2006.

Richardson, A. D., Bailey, A. S., Denny, E. G., Martin, C. W., and O'Keefe, J.: Phenology of a northern hardwood forest canopy, Glob. Change Biol., 12, 1174–1188, doi:10.1111/j.1365-2486.2006.01164.x, 2006.

Richardson, A. D., Keenan, T. F., Migliavacca, M., Ryu, Y., Sonnentag, O., and Toomey, M.: Climate change, phenology, and phenological control of vegetation feedbacks to the climate system, Agr. Forest Meteorol., 169, 156–173, 2013.

Rienecker, M. M., Suarez, M. J., Gelaro, R., Todling, R., Bacmeister, J., Liu, E., Bosilovich, M. G., Schubert, S. D., Takacs, L., Kim, G. K., Bloom, S., Chen, J. Y., Collins, D., Conaty, A., Da Silva, A., Gu, W., Joiner, J., Koster, R. D., Lucchesi, R., Molod, A., Owens, T., Pawson, S., Pegion, P., Redder, C. R., Reichle, R., Robertson, F. R., Ruddick, A. G., Sienkiewicz, M., and Woollen, J.: MERRA: NASA's Modern-Era Retrospective Analysis for Research and Applications, J. Climate, 24, 3624–3648, doi:10.1175/Jcli-D-11-00015.1, 2011.

Rosenzweig, C. and Abramopoulos, F.: Land-surface model development for the GISS GCM, J. Climate, 10, 2040–2054, doi:10.1175/1520-0442(1997)010<2040:Lsmdft>2.0.Co;2, 1997.

Sacks, W. J., Deryng, D., Foley, J. A., and Ramankutty, N.: Crop planting dates: an analysis of global patterns, Global Ecol. Biogeogr., 19, 607–620, doi:10.1111/J.1466-8238.2010.00551.X, 2010.

Schaefer, K., Collatz, G. J., Tans, P., Denning, A. S., Baker, I., Berry, J., Prihodko, L., Suits, N., and Philpott, A.: Combined Simple Biosphere/Carnegie-Ames-Stanford Approach terrestrial carbon cycle model, J. Geophys. Res., 113, G03034, doi:10.1029/2007jg000603, 2008.

Schaefer, K., Schwalm, C. R., Williams, C., et al.: A model-data comparison of gross primary productivity: Results from the North American Carbon Program site synthesis, J. Geophys. Res., 117, G03010, doi:10.1029/2012jg001960, 2012.

Schmidt, G. A., Ruedy, R., Hansen, J. E., Aleinov, I., Bell, N., Bauer, M., Bauer, S., Cairns, B., Canuto, V., Cheng, Y., Del Genio, A., Faluvegi, G., Friend, A. D., Hall, T. M., Hu, Y. Y., Kelley, M., Kiang, N. Y., Koch, D., Lacis, A. A., Lerner, J., Lo, K. K., Miller, R. L., Nazarenko, L., Oinas, V., Perlwitz, J., Perlwitz, J., Rind, D., Romanou, A., Russell, G. L., Sato, M., Shindell, D. T., Stone, P. H., Sun, S., Tausnev, N., Thresher, D., and Yao, M. S.: Present-day atmospheric simulations using GISS ModelE: Comparison to in situ, satellite, and reanalysis data, J. Climate, 19, 153–192, doi:10.1175/Jcli3612.1, 2006.

Schmidt, G. A., Kelley, M., Nazarenko, L., Ruedy, R., Russell, G. L., Aleinov, I., Bauer, M., Bauer, S. E., Bhat, M. K., Bleck, R., Canuto, V., Chen, Y. H., Cheng, Y., Clune, T. L., Del Genio, A., de Fainchtein, R., Faluvegi, G., Hansen, J. E., Healy, R. J., Kiang, N. Y., Koch, D., Lacis, A. A., LeGrande, A. N., Lerner, J., Lo, K. K., Matthews, E. E., Menon, S., Miller, R. L., Oinas, V., Oloso, A. O., Perlwitz, J. P., Puma, M. J., Putman, W. M., Rind, D., Romanou, A., Sato, M., Shindell, D. T., Sun, S., Syed, R. A., Tausnev, N., Tsigaridis, K., Unger, N., Voulgarakis, A., Yao, M. S., and Zhang, J. L.: Configuration and assessment of the GISS ModelE2 contributions to the CMIP5 archive, J. Adv. Model Earth Sy., 6, 141–184, doi:10.1002/2013ms000265, 2014.

Schuster, C., Estrella, N., and Menzel, A.: Shifting and extension of phenological periods with increasing temperature along ele-

vational transects in southern Bavaria, Plant Biol., 16, 332–344, doi:10.1111/Plb.12071, 2014.

Scott, C. E., Rap, A., Spracklen, D. V., Forster, P. M., Carslaw, K. S., Mann, G. W., Pringle, K. J., Kivekäs, N., Kulmala, M., Lihavainen, H., and Tunved, P.: The direct and indirect radiative effects of biogenic secondary organic aerosol, Atmos. Chem. Phys., 14, 447–470, doi:10.5194/acp-14-447-2014, 2014.

Shindell, D. T., Lamarque, J.-F., Schulz, M., Flanner, M., Jiao, C., Chin, M., Young, P. J., Lee, Y. H., Rotstayn, L., Mahowald, N., Milly, G., Faluvegi, G., Balkanski, Y., Collins, W. J., Conley, A. J., Dalsoren, S., Easter, R., Ghan, S., Horowitz, L., Liu, X., Myhre, G., Nagashima, T., Naik, V., Rumbold, S. T., Skeie, R., Sudo, K., Szopa, S., Takemura, T., Voulgarakis, A., Yoon, J.-H., and Lo, F.: Radiative forcing in the ACCMIP historical and future climate simulations, Atmos. Chem. Phys., 13, 2939–2974, doi:10.5194/acp-13-2939-2013, 2013a.

Shindell, D. T., Pechony, O., Voulgarakis, A., Faluvegi, G., Nazarenko, L., Lamarque, J.-F., Bowman, K., Milly, G., Kovari, B., Ruedy, R., and Schmidt, G. A.: Interactive ozone and methane chemistry in GISS-E2 historical and future climate simulations, Atmos. Chem. Phys., 13, 2653–2689, doi:10.5194/acp-13-2653-2013, 2013b.

Simard, M., Pinto, N., Fisher, J. B., and Baccini, A.: Mapping forest canopy height globally with spaceborne lidar, J. Geophys. Res., 116, G04021, doi:10.1029/2011jg001708, 2011.

Sitch, S., Smith, B., Prentice, I. C., Arneth, A., Bondeau, A., Cramer, W., Kaplan, J. O., Levis, S., Lucht, W., Sykes, M. T., Thonicke, K., and Venevsky, S.: Evaluation of ecosystem dynamics, plant geography and terrestrial carbon cycling in the LPJ dynamic global vegetation model, Glob. Change Biol., 9, 161–185, doi:10.1046/J.1365-2486.2003.00569.X, 2003.

Sitch, S., Cox, P. M., Collins, W. J., and Huntingford, C.: Indirect radiative forcing of climate change through ozone effects on the land-carbon sink, Nature, 448, 791–794, doi:10.1038/Nature06059, 2007.

Sitch, S., Friedlingstein, P., Gruber, N., Jones, S. D., Murray-Tortarolo, G., Ahlström, A., Doney, S. C., Graven, H., Heinze, C., Huntingford, C., Levis, S., Levy, P. E., Lomas, M., Poulter, B., Viovy, N., Zaehle, S., Zeng, N., Arneth, A., Bonan, G., Bopp, L., Canadell, J. G., Chevallier, F., Ciais, P., Ellis, R., Gloor, M., Peylin, P., Piao, S. L., Le Quéré, C., Smith, B., Zhu, Z., and Myneni, R.: Recent trends and drivers of regional sources and sinks of carbon dioxide, Biogeosciences, 12, 653–679, doi:10.5194/bg-12-653-2015, 2015.

Spitters, C. J. T., Toussaint, H. A. J. M., and Goudriaan, J.: Separating the Diffuse and Direct Component of Global Radiation and Its Implications for Modeling Canopy Photosynthesis, 1. Components of Incoming Radiation, Agr. Forest Meteorol., 38, 217–229, doi:10.1016/0168-1923(86)90060-2, 1986.

Stephenson, N. L. and van Mantgem, P. J.: Forest turnover rates follow global and regional patterns of productivity, Ecol. Lett., 8, 524–531, doi:10.1111/J.1461-0248.2005.00746.X, 2005.

Sugiura, D. and Tateno, M.: Optimal Leaf-to-Root Ratio and Leaf Nitrogen Content Determined by Light and Nitrogen Availabilities, Plos One, 6, e22236, doi:10.1371/journal.pone.0022236, 2011.

Thomas, R. Q., Zaehle, S., Templer, P. H., and Goodale, C. L.: Global patterns of nitrogen limitation: confronting two global

biogeochemical models with observations, Glob. Change Biol., 19, 2986–2998, doi:10.1111/Gcb.12281, 2013.

Thornton, P. E., Lamarque, J. F., Rosenbloom, N. A., and Mahowald, N. M.: Influence of carbon-nitrogen cycle coupling on land model response to CO_2 fertilization and climate variability, Global Biogeochem. Cy., 21, Gb4018, doi:10.1029/2006gb002868, 2007.

Unger, N.: Global climate impact of civil aviation for standard and desulfurized jet fuel, Geophys. Res. Lett., 38, L20803, doi:10.1029/2011gl049289, 2011.

Unger, N.: Isoprene emission variability through the twentieth century, J. Geophys. Res., 118, 13606–13613, doi:10.1002/2013jd020978, 2013.

Unger, N.: Human land-use-driven reduction of forest volatiles cools global climate, Nat. Clim. Change, 4, 907–910, doi:10.1038/Nclimate2347, 2014a.

Unger, N.: On the role of plant volatiles in anthropogenic global climate change, Geophys. Res. Lett., 41, 8563–8569, doi:10.1002/2014gl061616, 2014b.

Unger, N. and Yue, X.: Strong chemistry- climate feedbacks in the Pliocene, Geophys. Res. Lett., 41, 527–533, doi:10.1002/2013gl058773, 2014.

Unger, N., Harper, K., Zheng, Y., Kiang, N. Y., Aleinov, I., Arneth, A., Schurgers, G., Amelynck, C., Goldstein, A., Guenther, A., Heinesch, B., Hewitt, C. N., Karl, T., Laffineur, Q., Langford, B., A. McKinney, K., Misztal, P., Potosnak, M., Rinne, J., Pressley, S., Schoon, N., and Serça, D.: Photosynthesis-dependent isoprene emission from leaf to planet in a global carbon–chemistry–climate model, Atmos. Chem. Phys., 13, 10243–10269, doi:10.5194/acp-13-10243-2013, 2013.

Val Martin, M., Heald, C. L., and Arnold, S. R.: Coupling dry deposition to vegetation phenology in the Community Earth System Model: Implications 3 for the simulation of surface O_3, Geophys. Res. Lett., 8, 2988–2996, doi:10.1002/2014GL059651, 2014.

Vitasse, Y., Delzon, S., Dufrene, E., Pontailler, J. Y., Louvet, J. M., Kremer, A., and Michalet, R.: Leaf phenology sensitivity to temperature in European trees: Do within-species populations exhibit similar responses?, Agr. Forest Meteorol., 149, 735–744, doi:10.1016/J.Agrformet.2008.10.019, 2009.

von Caemmerer, S. and Farquhar, G. D.: Some Relationships between the Biochemistry of Photosynthesis and the Gas-Exchange of Leaves, Planta, 153, 376–387, 1981.

Weedon, G. P., Balsamo, G., Bellouin, N., Gomes, S., Best, M. J., and Viterbo, P.: The WFDEI meteorological forcing data set: WATCH Forcing Data methodology applied to ERA-Interim reanalysis data, Water Resour. Res., 50, 7505–7514, doi:10.1002/2014wr015638, 2014.

White, M. A., Thornton, P. E., and Running, S. W.: A continental phenology model for monitoring vegetation responses to interannual climatic variability, Global Biogeochem. Cy., 11, 217–234, doi:10.1029/97gb00330, 1997.

Wittig, V. E., Ainsworth, E. A., and Long, S. P.: To what extent do current and projected increases in surface ozone affect photosynthesis and stomatal conductance of trees? A meta-analytic review of the last 3 decades of experiments, Plant Cell Environ., 30, 1150–1162, doi:10.1111/J.1365-3040.2007.01717.X, 2007.

Yienger, J. J. and Levy, H.: Empirical-Model of Global Soil-Biogenic Nox Emissions, J. Geophys. Res., 100, 11447–11464, doi:10.1029/95jd00370, 1995.

Yue, X. and Unger, N.: Ozone vegetation damage effects on gross primary productivity in the United States, Atmos. Chem. Phys., 14, 9137–9153, doi:10.5194/acp-14-9137-2014, 2014.

Yue, X., Unger, N., Keenan, T. F., Zhang, X., and Vogel, C. S.: Probing the past 30 year phenology trend of US deciduous forests, Biogeosciences, in press, 2015a.

Yue, X., Unger, N., and Zheng, Y.: Distinguishing the drivers of trends in land carbon fluxes and biogenic emissions over the past three decades, Atmos. Chem. Phys., submitted, 2015b.

Zaehle, S., Medlyn, B. E., De Kauwe, M. G., Walker, A. P., Dietze, M. C., Hickler, T., Luo, Y. Q., Wang, Y. P., El-Masri, B., Thornton, P., Jain, A., Wang, S. S., Warlind, D., Weng, E. S., Parton, W., Iversen, C. M., Gallet-Budynek, A., McCarthy, H., Finzi, A. C., Hanson, P. J., Prentice, I. C., Oren, R., and Norby, R. J.: Evaluation of 11 terrestrial carbon-nitrogen cycle models against observations from two temperate Free-Air CO_2 Enrichment studies, New Phytol., 202, 803–822, doi:10.1111/Nph.12697, 2014.

Zeng, N., Mariotti, A., and Wetzel, P.: Terrestrial mechanisms of interannual CO_2 variability, Global Biogeochem. Cy., 19, Gb1016, doi:10.1029/2004GB002273, 2005.

Zhang, X. Y., Tan, B., and Yu, Y. Y.: Interannual variations and trends in global land surface phenology derived from enhanced vegetation index during 1982–2010, Int. J. Biometeorol., 58, 547–564, doi:10.1007/S00484-014-0802-Z, 2014.

Zhao, M. S. and Running, S. W.: Drought-Induced Reduction in Global Terrestrial Net Primary Production from 2000 Through 2009, Science, 329, 940–943, doi:10.1126/Science.1192666, 2010.

Zhao, M. S., Heinsch, F. A., Nemani, R. R., and Running, S. W.: Improvements of the MODIS terrestrial gross and net primary production global data set, Remote Sens. Environ., 95, 164–176, doi:10.1016/J.Rse.2004.12.011, 2005.

Zheng, Y., Unger, N., Barkley, M. P., and Yue, X.: Relationships between photosynthesis and formaldehyde as a probe of isoprene emission, Atmos. Chem. Phys., 15, 8559–8576, doi:10.5194/acp-15-8559-2015, 2015.

Zhu, Z. C., Bi, J., Pan, Y. Z., Ganguly, S., Anav, A., Xu, L., Samanta, A., Piao, S. L., Nemani, R. R., and Myneni, R. B.: Global Data Sets of Vegetation Leaf Area Index (LAI)3g and Fraction of Photosynthetically Active Radiation (FPAR)3g Derived from Global Inventory Modeling and Mapping Studies (GIMMS) Normalized Difference Vegetation Index (NDVI3g) for the Period 1981 to 2011, Remote Sens., 5, 927–948, doi:10.3390/Rs5020927, 2013.